Arabian Journal of Chemistry (2021) **14**, 103100

King Saud University

Arabian Journal of Chemistry

www.ksu.edu.sa
www.sciencedirect.com

ORIGINAL ARTICLE

Electrochemical investigations of hydrochloric acid corrosion for carbon steel and coating effect by Poly (butyl Methacrylate)-grafted alginate/Fe_3O_4

Eman Alzahrani, Hala M. Abo-Dief, Faouzia Algethami

Department of Chemistry, College of Science, Taif University, P.O. Box 11099, Taif 21944, Saudi Arabia

Received 19 October 2020; accepted 18 February 2021
Available online 2 March 2021

Abstract This study aimed at analyzing the performance of a corrosion resistant coating made from tri-iron tetraoxide (Fe_3O_4) nanoparticles (NPs) and (Butyl-2-methylprop-2-enoate)-grafted alignate/Fe_3O_4 nanocomposite. Two methods were used to characterize the combination; Thermo Gravimetric Analysis (TGA) and the Differential Scanning Calorimetry (DSC). It was observed that the rate of corrosion of the carbon steel was greatly influenced by the molarities of HCl used, temperature and time of immersion. Corrosion rate was found to increase with increase in molarity of the hydrochloric acid and temperature but was inversely proportional to the time of immersion. Carbon steel was coated with the corrosion resistant combination using the hot-dip coating method. To characterize the coating, Scanning Electron Microscope (SEM), Energy dispersive X-Ray (EDX), Fourier transform infrared (FT-IR) and X-Ray Diffraction (XRD) methods were used. Electrochemical studies (Tafel polarization and cyclic voltametry) showed that the optimum conditions for prevention of corrosion of the carbon steel were 150 °C and immersed time of 2 hrs. The efficiency of coating varied between the 2 combinations, with PBMA-gft-Alg/Fe_3O_4 nanocomposite being more effective than Fe_3O_4NPs coating.

1. Introduction

Coating to enhance mechanical strength and corrosion resistance is one of the best practical and cost effective methods for metallic components (Gray & Luan, 2002; Lin & Dahan, 2015). Carbon steels typically contain less than 1.5% carbon content along with the minute presence of Mn, Si, P and S. Based on the percentage of carbon, the classification is further divided into three forms, namely low carbon steels

E-mail addresses: em-s-z@tu.edu.sa (E. Alzahrani), h.abodeif@tu.edu.sa (H.M. Abo-Dief)
Peer review under responsibility of King Saud University.

Production and hosting by Elsevier

https://doi.org/10.1016/j.arabjc.2021.103100
1878-5352 © 2021 Published by Elsevier B.V. on behalf of King Saud University.

(< 0.25% C), medium carbon steels (0.25–0.70% C) and high carbon steels (0.70–1.05% C). Variation of the percentage of carbon content allows to attain different mechanical properties such as strength, ductility, hardness, *etc*. Based on the steel properties, related to carbon content, plain carbon steels are further divided into certain grades, such as grade 1008 (0.08 wt% C), which is good for forming and has good ductility; grade 1018 (0.18 wt% C), useful for general application and good for welding; grade 1030 (0.30 wt% C), which has low hardenability; grade 1045 (0.45 wt% C), which has applications in power transmission and shafting; and X-65, which is a seamless grade and weldable (Dwivedi et al., 2017; Wang et al., 2020). An economic study has shown that internal coating on pipelines or other structures is more cost effective than that of bare carbon steel plus inhibitors, (Radhamani et al., 2020). In a marine environment, steel corrosion is influenced by parameters such as salinity (concentration of dissolved salt), alkalinity (concentration of hydrogen ions) and hardness of sea water, (Radhamani et al., 2020). Steel corrosion of is basically an electrochemical reaction which occurs in the presence of water, O_2, and ions such as C^-or F^- ions, (Bertolini et al., 2004; Horwood). In corrosion, electrons get transferred from metals with greater negative potential and the corrosion occurs at the point from where the electrons leave, (Radhamani et al., 2020). Nano structured hydrophobic and super-hydrophobic coating of primers were explored to prevent steel corrosion, (Morton et al., 2018; Xiang et al., 2018; Zhang et al., 2016). (Ershad-Langroudi et al., 2017; Ledwig & Dubiel, 2017; Mora et al., 2017) found that in a typical nanocomposite coating, specific nanoparticles (NPs) are added to enhance the overall performance.

(Harb et al., 2020; Joshi et al., 2018) used organic polymer coating or paints with epoxy resins polyurethane (PU) and acrylic are widely used to prevent corrosion. (Cui et al., 2018; Mai & Yu, 2006; Nguyen-Tri et al., 2018) found that pristine polymer alone is insufficient in effectively preventing corrosion. (Peng et al., 2018; Qu et al., 2013) described many science disciplines influenced by nanotechnology. (Alam et al., 2018; and Guan et al., 2018) have found that organic/inorganic fillers have become prominent. (Radhamani et al., 2020) showed that fillers size, shape, morphology and the weight percent greatly influence the intrinsic properties of composites. (Morton et al., 2018; Xiang et al., 2018; Zhang et al., 2016) used nanostructured hydrophobic and super-hydrophobic coating to prevent steel corrosion and (Radhamani et al., 2020) found that specific nanoparticles (NPs) must be added to enhance the overall performance of the nanocomposite coating.

(Jagtap et al., 2018) improved nanocomposites thermal resistance, corrosion resistance and mechanical properties with both a high surface area and van der Waals' force of attraction. (Ramezanzadeh et al., 2016) concluded that hybrid coatings have the potential to open up a new scope especially in epoxy-based coatings. (Deyab, 2015) discussed the problems of the coating permeability and weak adhesion. (Sanchez et al., 2011) explored the combination of organic and inorganic coating is getting explored to make use of both their properties. (Elmorsi & Hassanein, 1999; Nagiub et al., 2013; Yusoff et al., 2020) have shown that the organic inhibition of the corrosion by dyes is mainly attributed to the formation of complex compounds between the metal-ions and the dye at the electrode surface. Their adsorption characteristics depend on

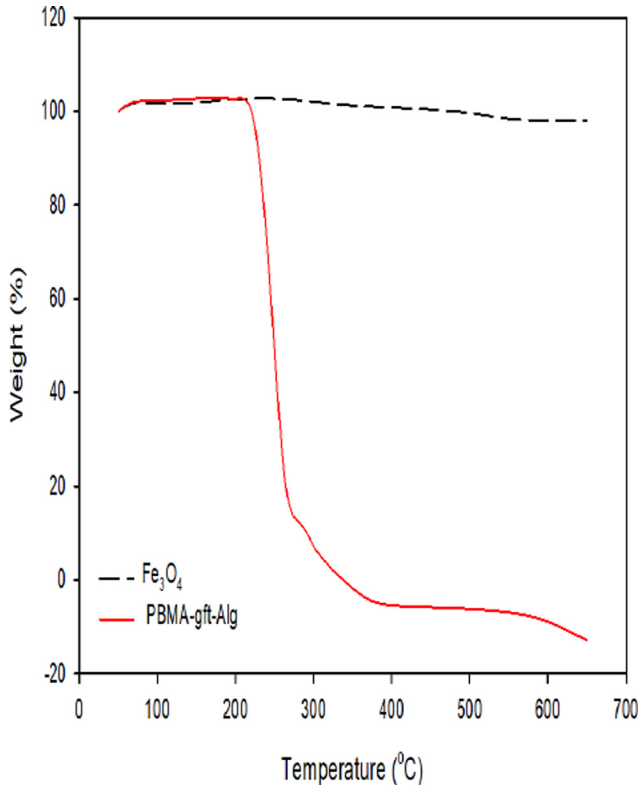

Fig. 1 TGA thermograms of Fe_3O_4 NPs and PBMA-gft-Alg.

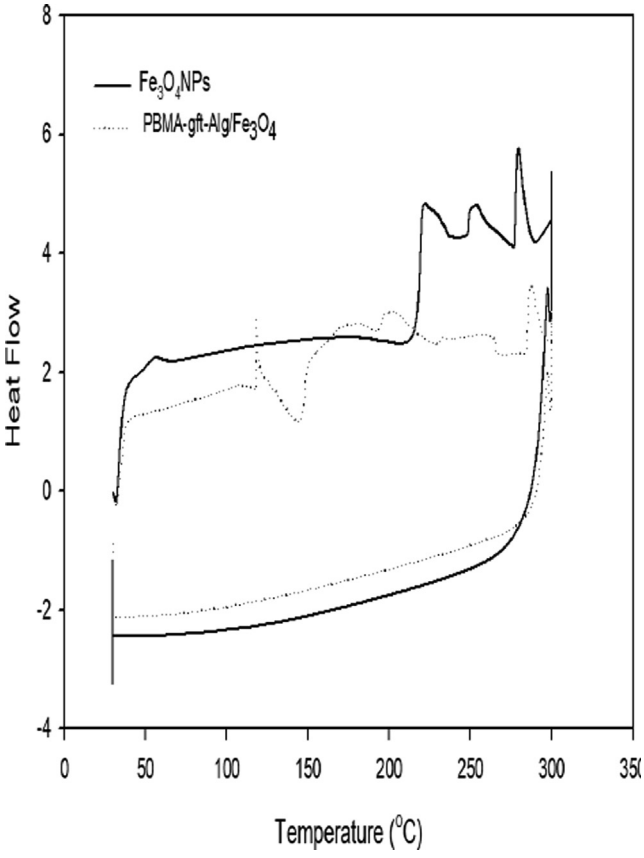

Fig. 2 DSC thermograms of Fe_3O_4 NPs and PBMA-gft-Alg/Fe_3O_4.

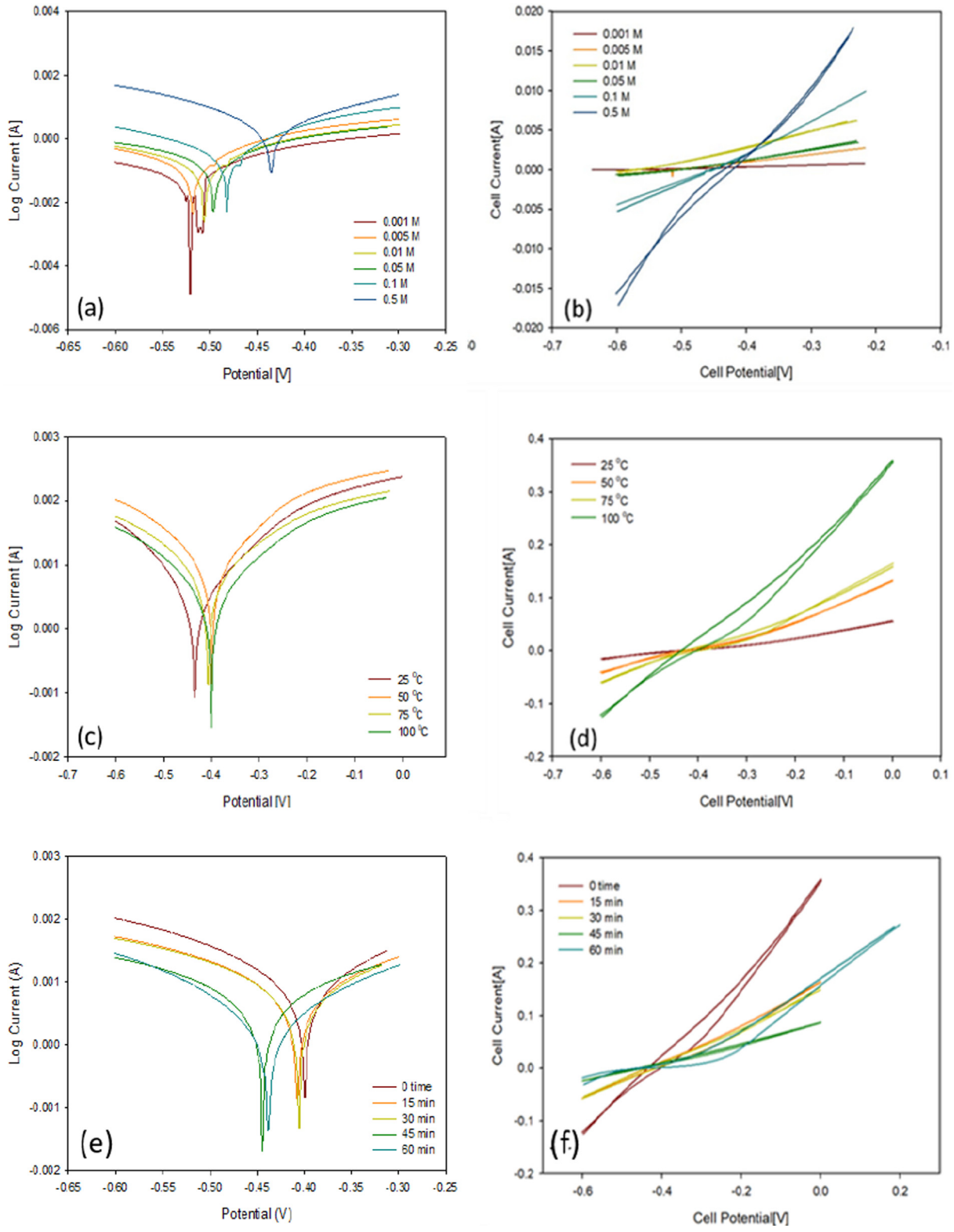

Fig. 3 Polarization curves and CV voltammograms of a carbon steel electrode immersed (a, b) in 0.001 to 0.5 M HCl, (c, d) in from 25 to 100 °C and (e, f) at 0 to 60 min.

Table 1 Potentiodynamic electrochemical parameters for the corrosion of carbon steel immersed in HCL.

		i_{corr} (A cm^{-2})	E_{corr} (V)	Slope (A/V)	Eh	Ep
Concentration (M)	0.001	0.00036	−0.567	0.002	−0.334	−0.526
	0.005	0.00037	−0.542	0.008	−0.382	−0.589
	0.01	0.00038	−0.529	0.018	−0.287	−0.517
	0.05	0.00115	−0.517	0.011	−0.319	−0.532
	0.1	0.00905	−0.423	0.037	−0.323	−0.464
	0.5	0.00905	−0.423	0.085	−0.382	−0.242
Temperature (°C)	25	0.00671	−0.403	0.085	−0.382	−0.242
	50	0.01	−0.395	0.272	−0.120	−0.540
	75	0.0144	−0.398	0.347	−0.180	−0.483
	100	0.0144	−0.398	0.768	0.001	−0.535
Time (min)	0	0.00703	−0.403	0.768	0.001	−0.535
	15	0.00633	−0.403	0.380	0.999	−0.192
	30	0.00448	−0.436	0.340	0.997	−0.182
	45	0.00390	−0.426	0.189	0.996	−0.461
	60	0.00036	−0.574	0.378	0.989	−0.463

several factors including the nature and number of potential adsorption sites present in the dye molecule. But, (Oguzie et al., 2006) found that adsorption of such dyes on the metal surface can distinctly alter the corrosion susceptibility, thus elucidation of the correlation between inhibitor adsorption and corrosion resistance is of immense importance.

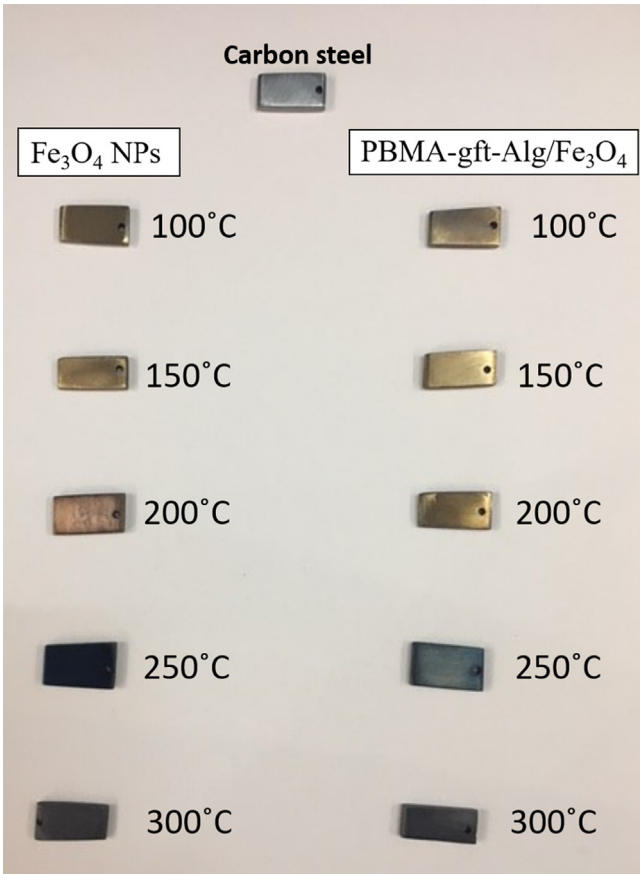

Fig. 4 Morphologies of carbon steel after coating by Fe_3O_4 NPs and PBMA-gft-Al/Fe_3O_4 at different temperature from 100 to 300 °C.

(Ye et al., 2020) showed that the inhibition efficiency of three carbon dots exceeded 90% at 200 mg/L and the highest inhibitive efficiency was found for the carbon dots prepared at the reaction time of 2 h and (Ye et al., 2020) found that the inhibition efficiency of carbon steel reached up to 93.93% (1 M HCl) and 88.96% (3.5 wt% NaCl) at 200 mg/L of N-CDs. (Aslam et al., 2020) found that The inhibition efficiency of IOD for mild steel in 1 M HCl was increased by rising its concentration attaining maximum value (96.6%) at 300 ppm at 30 °C and decreases with increasing temperature from 30 °C to 60 °C. (Ahmaeed et al., 2019) found that sodium iodide (NaI) Maximum inhibition efficiency was 96.1% at a higher level of inhibitor concentration, time and temperature in mild steel and 1 M HCl. (Hu et al., (2017) concluded that the macromolecule DNA protected carbon steel against 1 M HCl solution with the maximum inhibition efficiency reached 91.9%. (Haque et al., 2017) evaluated Aliquat 336 as a green and novel corrosion inhibitor for mild steel in a 1 M HCl solution with maximum inhibition efficiency of 94.6% at a very low concentration of 4.95 μM. (Srivastava et al., 2017) presented AIZ-3 inhibitor with maximum inhibition efficiency (IE) of 96.08% at a concentration as low as 0.55 mM (200 ppm) in 1 M HCl.

This investigative study was aimed at analyzing the effectiveness of a corrosion resistant coating composed of iron (III) nanoparticles and nanocomposite. To characterize the combination, both TGA and DSC methods were used. The carbon steel was coated with the combination. Coating characterization was done using SEM, XRD, EDX and FT-IR. The effect of the coating on the hydrochloric acid, MG, MB and formation water corrosion is discussed using Tafel and cyclic voltammetry methods.

2. Experiment

2.1. Chemicals/Materials

98% $FeSO_4{\cdot}7H_2O$ (RFM 151.91), HCl, NaOH, CH_3OH (methanol), C_2H_5OH (ethanol), C_2H_4 (ethene), dimethylcrylate (EDMA, 98%), sodium alignate, $NaNO_3$ (RFM 84.99), potassium peroxydisulfate (RFM 270.31), Butyl methacrylate (BMA, 99%), formation water. Carbon steel working elec-

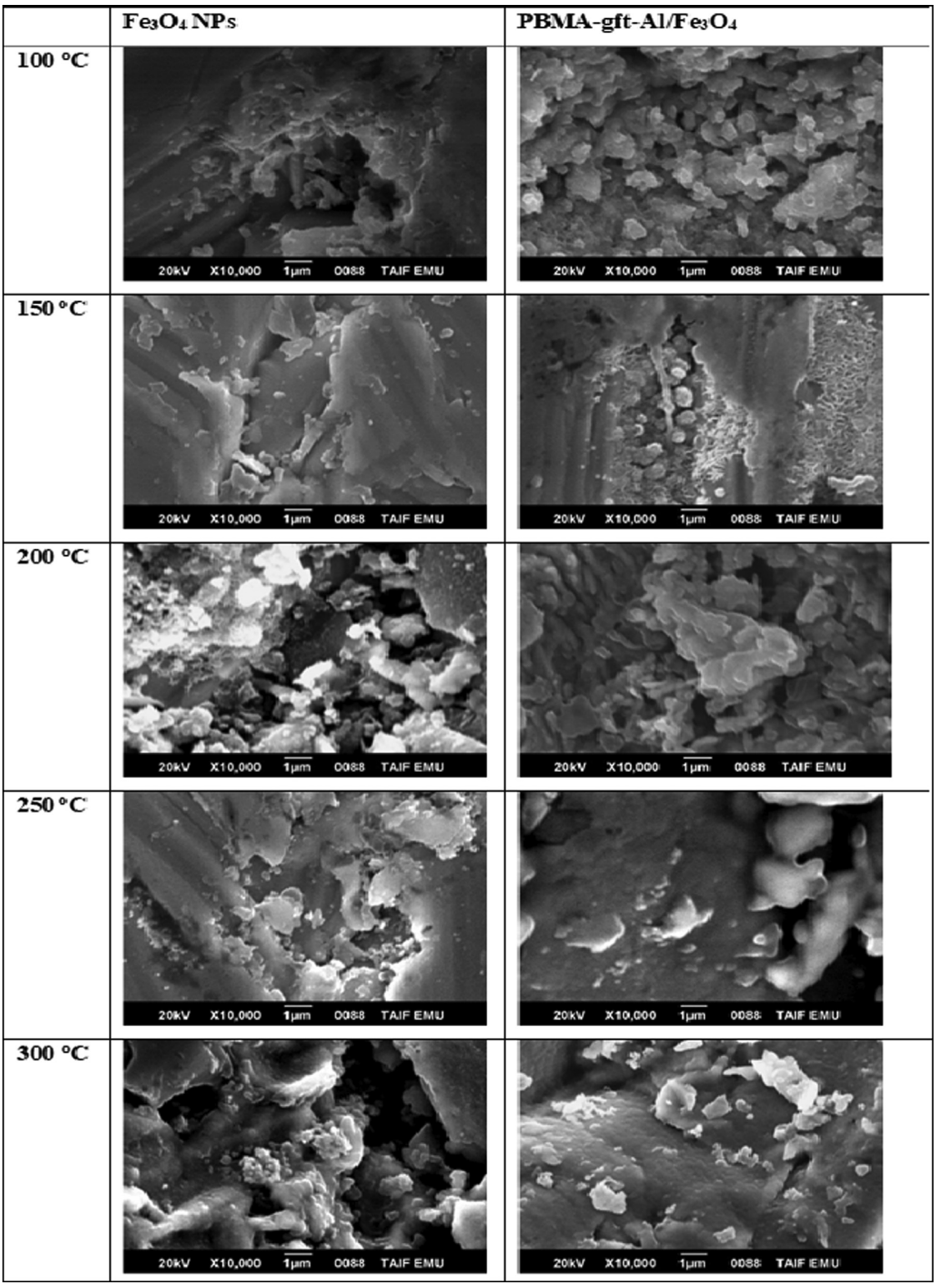

Fig. 5 SEM micrographs of a carbon steel surface after coating by Fe_3O_4 NPs and PBMA-gft-Al/Fe_3O_4 at different temperature from 100 to 300 °C.

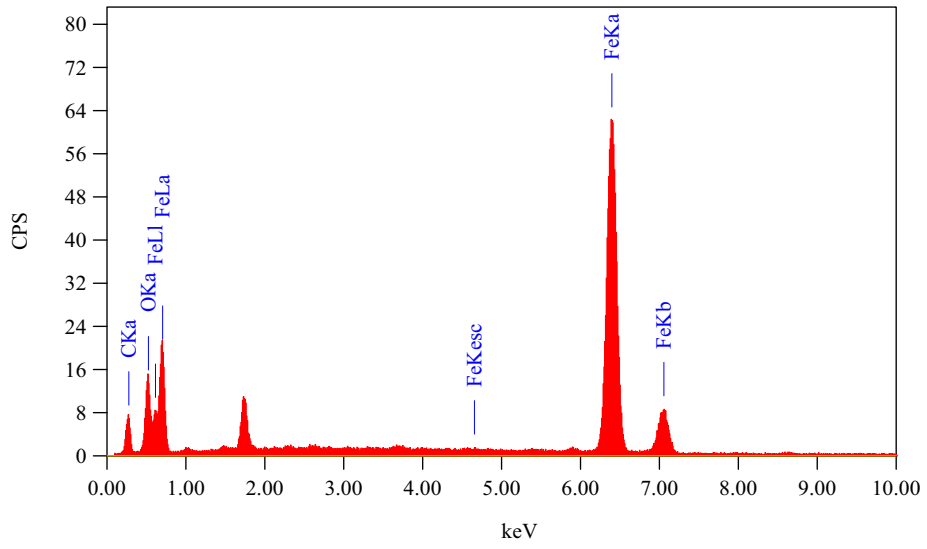

(a) Fe_3O_4 NPs at 100^{O}C.

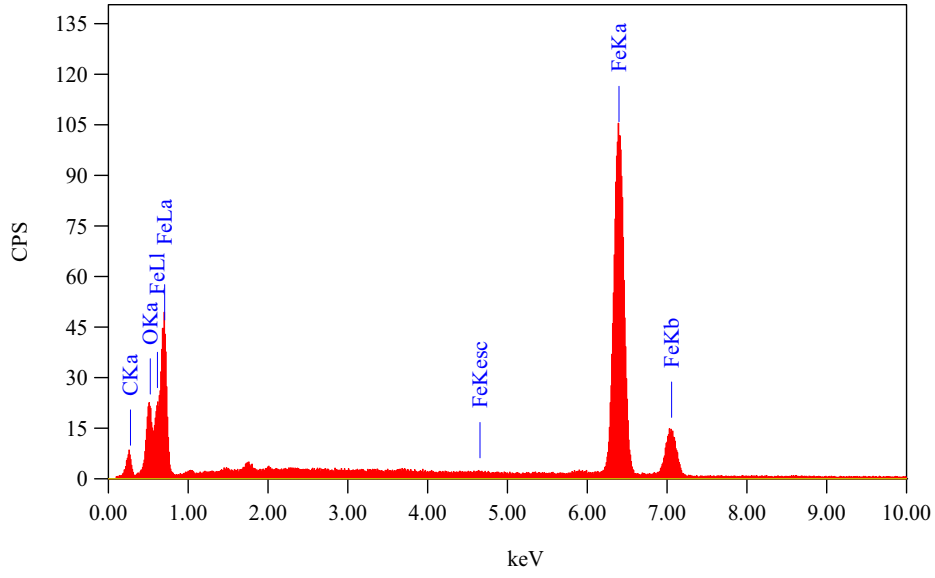

(b) PBMA-gft-Al/Fe_3O_4 at 100^{O}C.

Fig. 6 EDS spectra related to surface of carbon steel after coating by Fe3O4 NPs PBMA-gft-Al/Fe3O4 at different temperature from 100 to 300 °C.

trode (WE) of surface area 1 cm^2 containing 99.12% iron and the rest is carbon (0.06%), silicon (0.06%), manganese (0.005%), phosphorus (0.001%), sulphur (0.012%), nickel (0.015%), chromium (0.004%), molybdenum (0.002%), vanadium (0.02%) and copper (0.02%). Platinum and calomel are used as counter electrode (CE) and reference electrode (RE) respectively. Stock solutions were prepared by dissolving suitable quantities of dyes in distilled water.

2.2. Instruments

JEOL JSM 6390 Scanning electron microscope, D8-advance CuKá1-radiation diffractometer and pH meter are used. PerkinElmer RX FT-IR X2 used to provide FT-IR spectra (collected in ATR mode). Thermo Gravimetric Analysis (TGA) Mettler. Magnetic stirrer, an oven and a blast furnace. EZstat Propotentiostat (from NuVant Systems Inc. manufacturer, USA).

2.3. Synthesis of Fe_3O_4 and PBMA-gft-Alg/Fe_3O_4

Fe_3O_4 was prepared as described earlier (Alzahrani et al., 2020). To obtain Fe_3O_4 NPs, 3.3 g of iron (II) sulphate heptahydrate. was mixed with 2 g of sodium nitrate, dissolving the mixture in 50 cm^3 of distilled water then mixing the solution obtained with 20 cm^3 of 2.5 M NaOH solution. The mix-

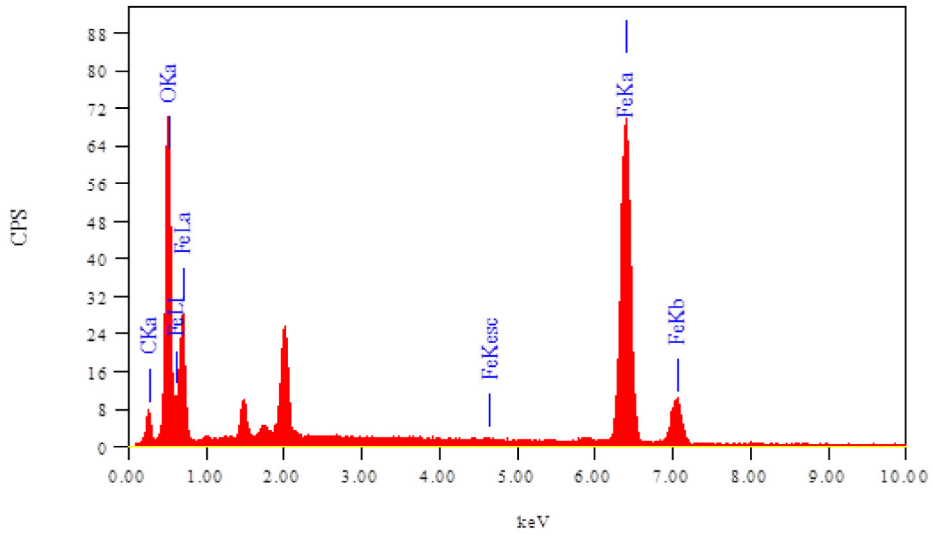

(c) Fe_3O_4 NPs at 150^{O}C.

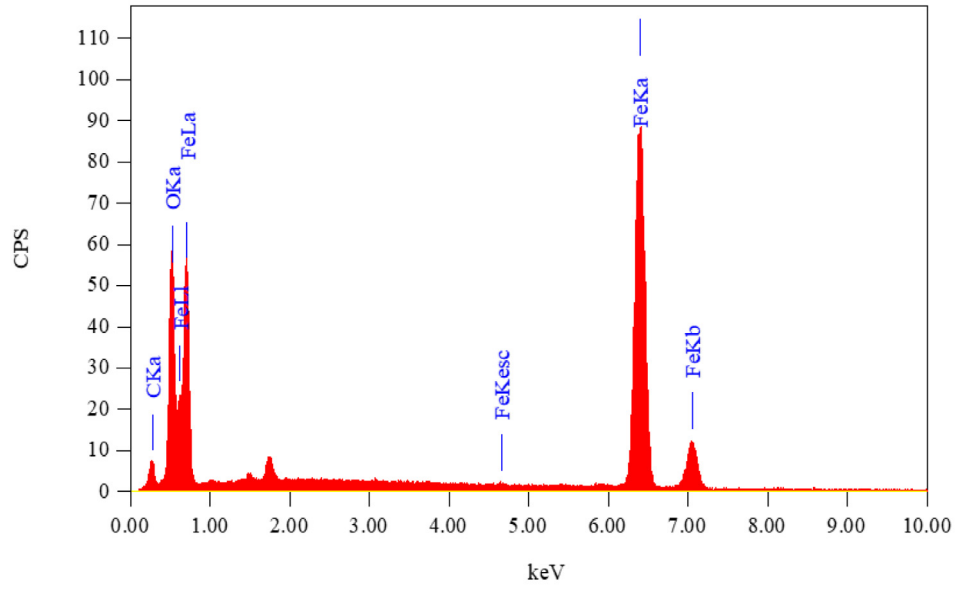

(d) PBMA-gft-Al/Fe_3O_4 at 100^{O}C.

Fig. 6 (*continued*)

ture was then heated to 80 °C while stirring constantly to ensure growth of the nanoparticle crystals. The reaction was allowed to proceed for 30 min before being cooled. The suspension formed was filtered and washed in distilled water to remove any unreacted chemicals. The Fe_3O_4 NPs, being magnetic, were separated from this mixture by use of a magnet before being dried overnight in an oven maintained at 50 °C before the coating process.

The nanocomposite were prepared as described in our previous work (Alzahrani et al., 2020). First, Ig of the Fe_3O_4 NPs prepared from the previous procedure was placed in 100 mL of de-ionized water and dispersed by use of a sonicator for a period of 30 min. This was followed by addition of alignate made by dissolving 2 g of the alignate in 200 mL of de-ionized water at 40 °C. 0.75 g of EDMA was mixed with 20 mL of BMA monomer at 60 °C and stirred continuously for 1hr. This was followed by addition of the Fe_3O_4 NPs dispersion, and 20 cm^3 of KPS (with 3% concentration) solution acting as initiator. The reaction was left to proceed for further 6hrs at 60 °C to form a nanocomposite which is then mixed with excess methyl alcohol in order to stop any further polymerization. The resulting product is filtered and washed thoruoghly

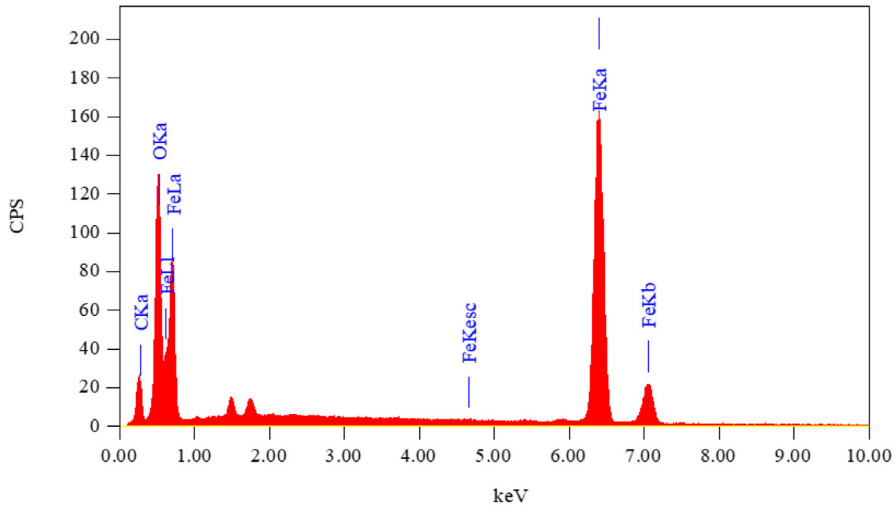

(e) Fe_3O_4 NPs at 200^{O}C.

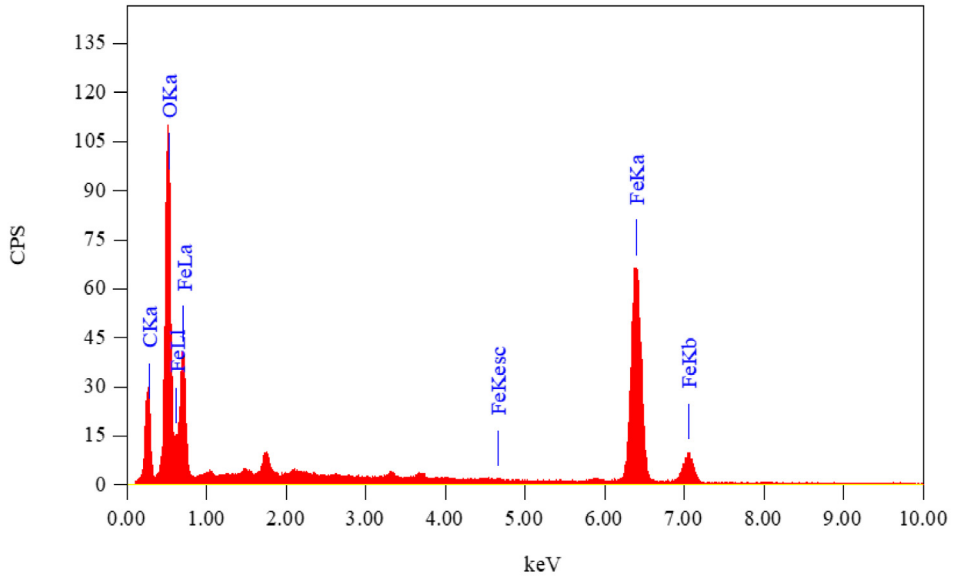

(f) PBMA-gft-Al/Fe $_3O_4$ at 200^{O}C.

Fig. 6 (*continued*)

in distilled water followed by drying in an oven at 60 °C for 2 hrs. The resultant product is ground and sieved to obtain final product.

2.4. Measurement of corrosion resistance

To measure corrosion performance, carbon steel sealed with epoxy resin was used as a working electrode. Only the sealed area was exposed to the hydrochloric acid electrolyte. Concentration of the acid and temperature were varied at (0.001, 0.005, 0.01, 0.05, 0.1 and 0.5 M) and (25, 50, 75 and 100 °C) respectively while time was varied at (0, 15, 30, 45 and 60 min) to study the extent of corrosion. Before measurements, the electrodes were ground down to 300, 400, 600, 800, 1200 and 2000 using a series of emery papers, washed in distilled water and dried using ethanol. A potentioscan was used to draw the potentiodynamic current–potential curves. The curves obtained by linear change from − 0.6 V (stating potential) upwards in reference to SCE but within 20 mVs^{-1} (the required scan rate), to the end of experiment (Keera & Deyab, 2005; Ye et al., 2021).

The nanoparticle and nanocomposite (Fe_3O_4 NPs and PBMA-gft-Alg/Fe_3O_4) materials were coated on the carbon steel by dipping the carbon steel electrodes in molten forms

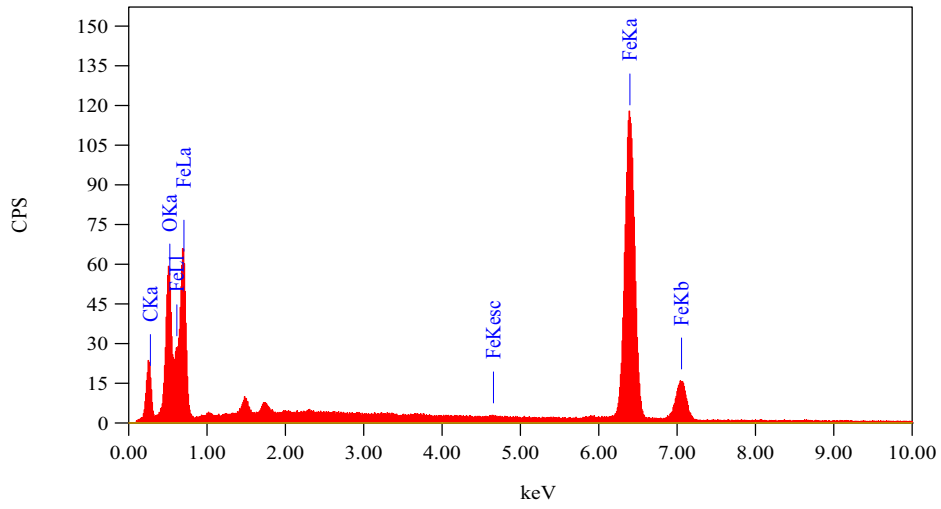

(g) Fe_3O_4 NPs at 250^{O}C.

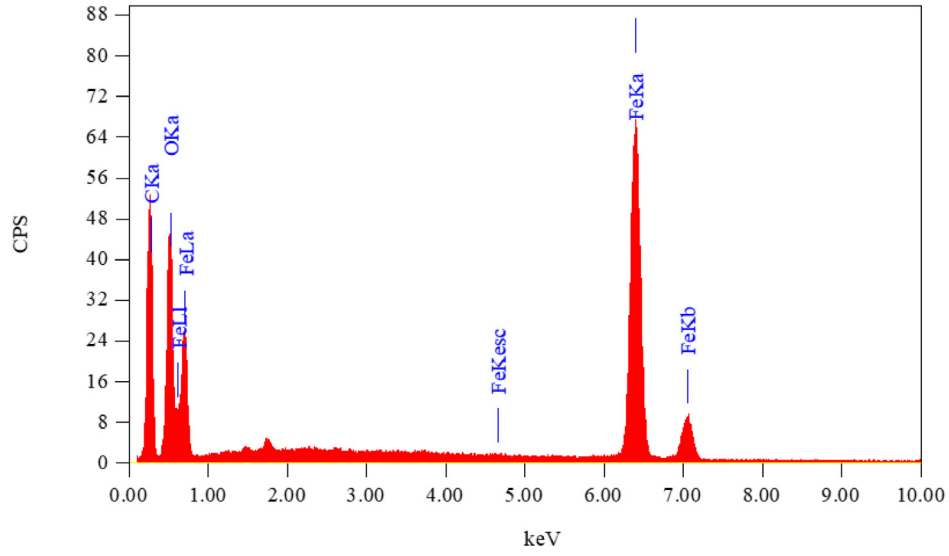

(h) PBMA-gft-Al/Fe_3O_4 at 250^{O}C.

Fig. 6 (*continued*)

of the materials (hot-dip method). The effect of varying temperatures (100, 150, 200 and 250 °C) and time (1, 2 and 3 hrs) were studied at optimum temperature of 150 °C. Characterization of the coating was achieved using FT-IR, cyclic voltammetry, EDX, X-ray diffraction, SEM, and Tafel polarization.

2.5. Assessment using formation water/dyes

Analysis of the formation water in the first test was done using the ion chromatography equipment and its chemical composition; 67,675Na^{+}, 127 K^{+}, 7708 Ca^{+2}, 2449 Mg^{+2}, 132,118Cl^{-}, 370 SO_4^{-2}, 568 Br^{-}, 11.8 SiO_4^{-2} and 6.7 pH. Test solution 2 was dyes carried out on MG/MB at pH = 10. The tests used the carbon steel coated with the nanocomposite at optimum conditions. Measurement was done at high corrosive condition.

3. Results and discussions

3.1. Characterization of the materials

Fig. 1 illustrates TGA curves representing Fe_3O_4 NPs weight loss as a result of residual water loss over temperature range between 50 °C and 650 °C in agreement with (Hussein-Al-Ali et al., 2014). According to the TGA thermogram, the alignate had a rapid weight loss at 230 °C with rate decrement at 271 °C which became constant at 350 °C. At 510 °C the alignate became at stable state continously. The weight decrease from 230 °C to 350 °C indicated the alignate decomposition within

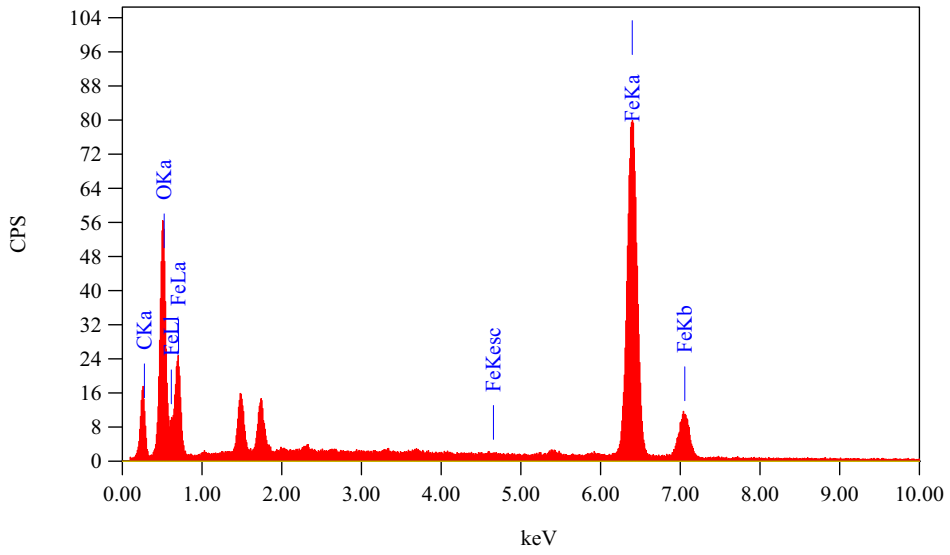

(i) Fe_3O_4 NPs at 300^{O}C.

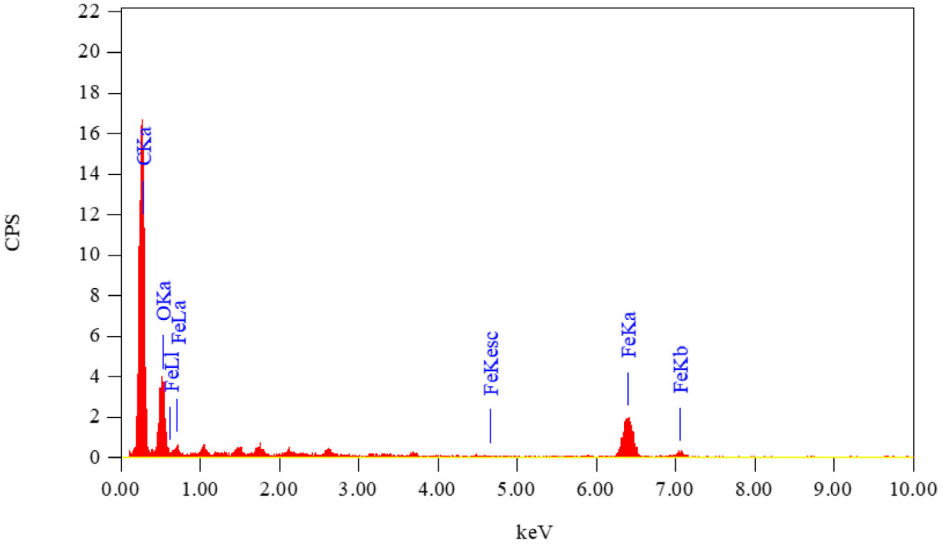

(j) PBMA-gft-Al/Fe $_3O_4$ at 300^{O}C.

Fig. 6 (*continued*)

this range of temperatures. Above 350 °C, the weight loss decreased due to the PBMA (poly Butyl methacrylate) decomposition in agreement with (Yao et al., 2010).

Fig. 2 illustrates an analysis of (Fe_3O_4 NPs and PBMA-gft-Alg/Fe_3O_4 repectively) using differential scanning calorimetry. Due to the solvent molecule elimination, the nanoparticles of Fe_3O_4 have a strong endothermic peak at 60 °C. Crystallization of the magnetite is responsible for the endothermic transition at 210 °C. The nano composite (PBMA-gft-Alg/Fe_3O_4) has even higher endothermic peak of about 115 °C.

Exothermic peaks observed at 140 °C and 190 °C due to crystallization and rearrangement of the molecules. This temperature range allowed crystallization of the powder as it allows the Fe_3O_4 NPs to interact strongly with the PBMA-gft-Alg/Fe_3O_4 nano composite. Secondly, the temperature rise resulted from the re-arranging of alignate and PBMA(poly Butyl methacrylate) groups themselves. These observations largely agree with the thermogravimetric analysis (Sneha & Sundaram, 2015).

3.2. Measurement of corrosion

3.2.1. Effect of the acid (HCl) concentration

Fig. 3a showed potentiodynamic polarization curves at varying hydrochloric acid concentrations. Table 1 illustrated Potentiodynamic electrochemical parameters for the corrosion

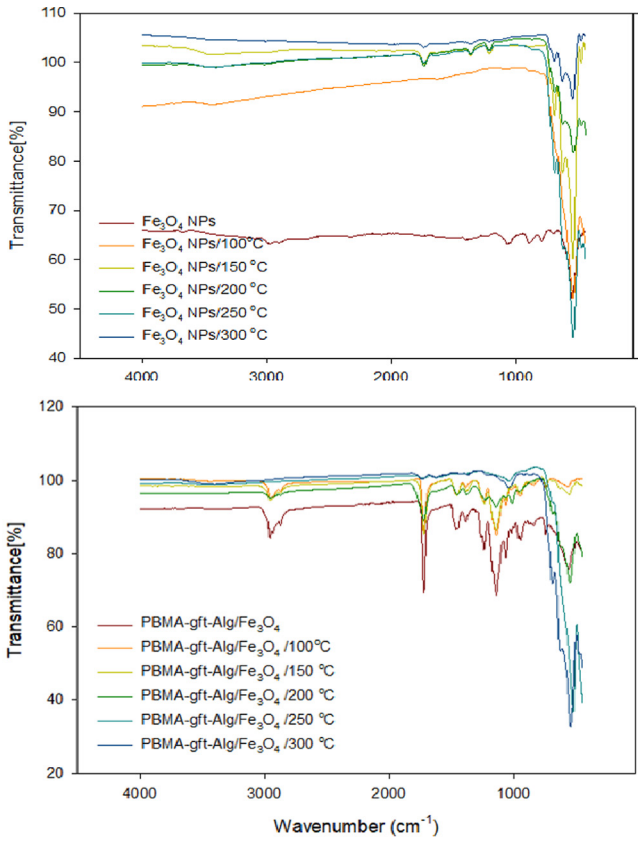

Fig. 7 FT-IR of Fe_3O_4 NPs, and PBMA-gft-Al/Fe_3O_4 at different temperature hot-dib coating.

of carbon steel. According hydrochloric acid concentration increment the anodic and cathodic branches towards values of high corrosion current density that causing significant rise in rate of corrosion. The i_{corr} values of carbon steel found to be directly proportional to the acid concentration which indicated the carbon steel higher corrosion effect with acid concentrations increment according to Fig. 1a and 3b and 1a in agreement with (Osarolube et al., 2008; Tang et al., 2011).

3.2.2. Effect of temperature

Fig. 3c showed the potentiodynamic polarization curves obtained at varying hydrochloric acid temperatures using carbon steel electrode. Table 1 showed the calculated values of the electrochemical parameters E_{corr} and i_{corr}. As the acid solution temperature increases, both the anodic and cathodic branches shifts towards values indicating high corrosion current density which causes a significant rise in rate of corrosion as indicated in Fig. 3d and Table 1, at 100 °C, and 0.5 M.

3.2.3. Effect of time

Fig. 3e showed the potentiodynamic polarization curves at various immersed time periods at both higher concentration and temperature values, while Table 1c shows values E_{corr} and i_{corr} values calculated from the curves. As the immersed time decreases, the branches shift to small current towards values of small corrosion current density, causing decrease in rate of corrosion. The i_{corr} inversely proportional to time, as shown in Fig. 3f and Table 1. The slope of the loop (carbon steel loop) is highest at 100 °C and 0 time which showed high corrosive effect in agreement with (Fawzy et al., 2018).

3.3. Coating

Carbon steel dipped in molten Fe_3O_4 NPs and PBMA-gft-Alg/Fe_3O_4 for a period of 1hr to coat it with the material. It subjected to heat from an oven (100, 150, 200, and 250 °C) in varying periods of time (1, 2 and 3 hrs.).

3.3.1. Effect of temperature and time

The corrosion process before and after coating monitored using Tafel polarization and cyclic voltammetry. FT-IR and XRD methods used to observe the morphology of the surface and chemical composition of the carbon steel as a result of temperature variations. Fig. 4 illustrated the carbon steel surface morphology of after coating at temperature and time values between 100 and 300 °C and 1 to 3 hrs. respectively.

3.3.2. Surface morphology

Fig. 5 showed particles and clustering with uniform distribution of nanoparticles after the hot-dip application method.

3.3.3. EDX Analysis

Fig. 6 illustrated the EDX analysis of the coated carbon steel (coating done at 100, 150, 200, and 250 °C). The spectra confirmed presence of carbon (C), Iron (Fe) and oxygen (O) in the coat. It is observed that with 150 °C temperature rise, the PBMA-gft-Alg/Fe_3O_4 carbon content increased while that in Fe_3O_4 NPs did not change. This agrees with the TGA curves in Fig. 1.

3.3.4. Fourier transforms infrared spectroscopy

Fig. 7 illustrated a band of high intensity for Fe_3O_4 NPs at (blank, 100, 150, 200, 250, and 300 °C). The absorption band of 580–630 cm^{-1} showed presence of Fe_3O_4NPs , more so for iron-oxygen (Fe-O) bond in Fe_3O_4 at 553 cm^{-1} (Bordbar et al., 2014; Waldron, 1955).

The spectrum for PBMA-gft-Alg/Fe_3O_4 at (blank, 100, 150, and 200 °C) is illustrated in Fig. 7b. Acrylate carboxyl group indicated by 1,730 cm^{-1} band. The presence of C–H and hence $–CH_3$ indicated by the band at 1,458 cm^{-1} while 2,985 cm^{-1} and 2,937 cm^{-1} bands indicated the stretching vibrations of C–H bonds in $–CH_3$ and $–CH_2$ in that order (Mittal et al., 2016). The peaks obtained at 250 and 300 °C were identical to those observed in Fe_3O_4 NPs but not visible in the PBMA and the alginate.

3.3.5. X-ray diffraction

Fig. 8 illustrated Fe_3O_4 NPs XRD. Diffraction peaks positions / relative intensities relations were at 2θ = 30.35, 35.68, 43.35, 54.70, 57.29, 62.82 and 74.30 assigned to (220), (311), (400), (422), (511), (440), and (533) reflections respectively indicating the presence of pure cubic spinel structure. Similar peaks observed in Fig. 8b, indicating the Fe_3O_4 NPs crystalline phase stability. Amorphous PBMA indicated by broad peak 2θ values at 17° for (blank 100, and 150 °C). The results indicated that PBMA-gft-Alg/Fe_3O_4 nanocomposite successfully synthesized (Bashtani et al., 2018). The peaks, however, do not rep-

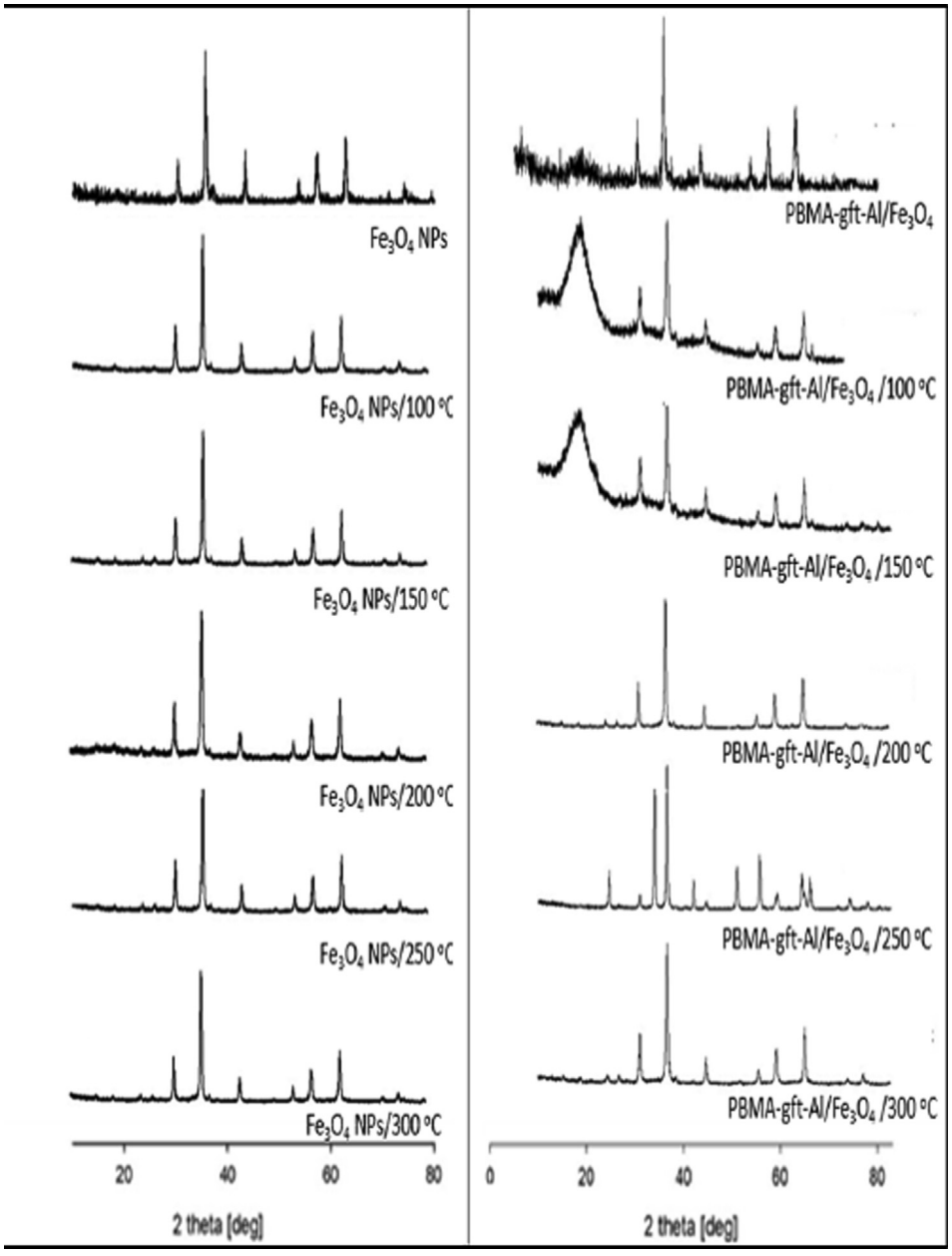

Fig. 8 X-ray diffraction patterns of Fe_3O_4 NPs and PBMA-gft-Alg/Fe_3O_4 at different temperature hot-dib coating.

resent XRD spectrum at (200, 250, and 300 °C) due to melting formation in agreement with TGA curves.

3.3.6. *Potentiodynamic polarization measurements*

Fig. 9 indicated the carbon steel potentio-dynamic polarization curves for the electrode at pre- and post-coating with the (Fe_3O_4 NPs and PBMA-gft-Al/Fe_3O_4) nanoparticles and the nanocomposite at (100, 150, 200, 250, and 300 °C) using 0.5 M of the hydrochloric acid electrolyte at a temperature of 150 °C and time 0. Table 2 showed E_{corr}, i_{corr}, cathodic and anodic Tafel values calculated from the curves. Polarization measurements used to calculate coating efficiency (PE %) using the equation:

$$PE\% = [(i_{corr}(coating) - i_{corr}(uncoating))/i_{corr}(coating)] \times 100$$

i_{corr} *(uncoating)* – Corrosion current density value before coating

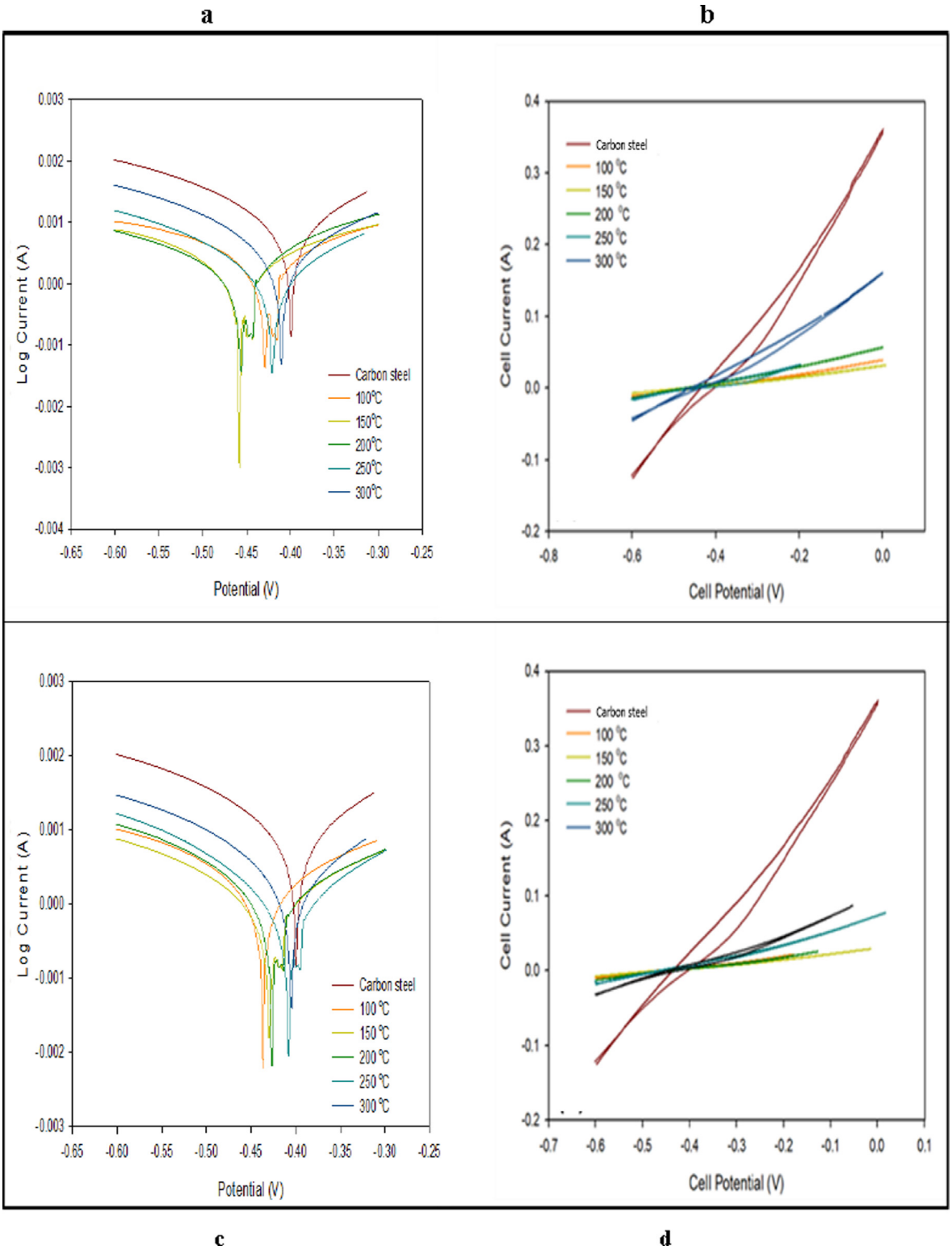

Fig. 9 Polarization curves and CV voltammograms of a carbon steel electrode in the absence and presence of coating by Fe_3O_4 NPs (above) and PBMA-gft-Alg/Fe_3O_4 (bottom) at different temperature at high corrosive condition.

Table 2 Potentiodynamic polarization parameters for corrosion carbon steel electrode in the absence and presence of coating by Fe_3O_4 NPs and PBMA-gft-Alg/Fe_3O_4 at different temperature at high corrosive condition.

		E_{corr} (V)	i_{corr} (A cm^{-2})	IE%	Slope (A/V)	E_h (V)	E_p (V)
Carbon steel		−0.398	0.01440	–	0.78	0.001	−0.535
Carbon steel coating by Fe_3O_4 NPs at	100 °C	−0.430	0.00239	83.4	0.80	−0.008	−0.601
	150 °C	−0.454	0.00190	86.7	0.06	−0.002	−0.601
	200 °C	−0.470	0.00220	84.6	0.11	−0.001	−0.532
	250 °C	−0.417	0.00280	80.5	0.11	−0.197	−0.504
	300 °C	−0.398	0.00549	61.0	0.33	−0.005	−0.544
Carbon steel coating by PBMA-gft-Alg/Fe_3O_4 at	100 °C	−0.425	0.00199	86.0	0.07	−0.178	−0.559
	150 °C	−0.418	0.00123	91.0	0.05	−0.119	−0.485
	200 °C	−0.398	0.00162	88.0	0.07	−0.128	−0.489
	250 °C	−0.402	0.00208	85.5	0.14	0.016	−0.492
	300 °C	−0.405	0.00416	71.0	0.20	−0.051	−0.555

i_{corr} *(coating)* – Corrosion current density value after coating

Fig. 9, showed that the coated nanoparticles or nanocomposite shifted to the lower current densities with more negative potential values. At 150 °C, the nanocomposite had a higher efficiency which resulted from higher coating values. Fig. 9b and Table 2 showed the lowest slope of the nanoparticles coated carbon steel at 150 °C indicating the uppermost polarization and corrosion resistance. (Ibrahim & Bakdash, 2014).

3.3.7. *Effect of time*

Tafel polarization and cyclic voltammetry illustrated Pre and post coating monitoring of corrosion. Coating was, as before, done using the nanoparticles and nanocomposite. FT-IR and XRD methods used to investigate surface morphology and chemical composition. This used to understand the effect of time on the carbon steel surface morphology at 150 °C and (1, 2 and 3 hrs.) as indicated in Fig. 10.

3.3.7.1. Surfaces analysis (SEM). SEM imaging used to obtain the surface morphology of the carbon steel before and after coating. A more clear observation of clustering shape and nanoparticles distribution on the carbon steel surface illustrated in Fig. 11. High homogeneity of the NPs observed at 3 hrs. coupled with lower surface sticking. Homogeneity and surface sticking was higher in the case of nanocomposites at 2 hrs. However, the time increment decreased the homogeneity because of the carbon content increment due to its burning.

3.3.7.2. EDX Analysis. Fig. 12. Showed EDX analysis of the coated carbon steel with the naoparticles and the nanocomposite at (100, 150, 200, 250, and 300 °C). The spectra indicated the presentation iron and oxygen in the coating. The nanocomposite spectra showed the presence of carbon in which its amount increases with temperature increment as a result of its degradation in agreement with TGA curves shown Fig. 1.

3.3.7.3. Fourier transforms infrared spectroscopy. Fig. 13a showed naoparticles high intensity band of before being used in coating at (1, 2 and 3 hrs.). The absorption band from 580 cm^{-1} to 630 cm^{-1} indicated the presence of Fe–O bond

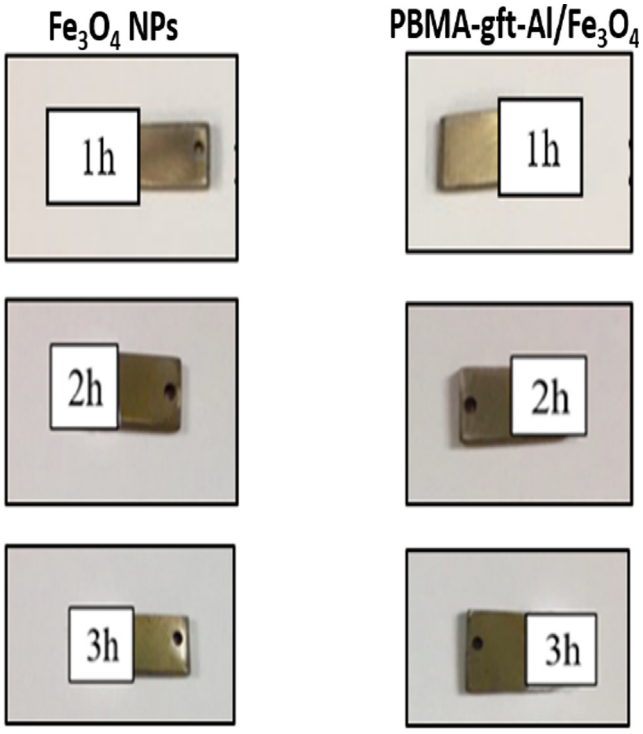

Fig. 10 Morphologies of carbon steel after coating by Fe_3O_4 NPs and PBMA-gft-Al/Fe_3O_4 at different time.

in Fe_3O_4 (at 553 cm^{-1}) nanoparticles (Bordbar et al., 2014; Waldron, 1955). The presence of $–CH_3$ and precisely for the C–H of the methyl group indicated by the 1,458 while the presence of acrylate carboxyl group indicated by the 1,730 cm^{-1} band (Mittal et al., 2016).

3.3.7.4. X-ray diffraction. Fig. 14 showed the Fe_3O_4NPs before coating the carbon steel at (1, 2 and 3 hrs.). The Fe_3O_4 cubic spinel crystal guided by the diffraction peak at 2θ. The position and relative intensities of the PBMA-gft-Alg/Fe_3O_4 peaks observed before coating at (1, 2 and 3 hrs.) diffractions are

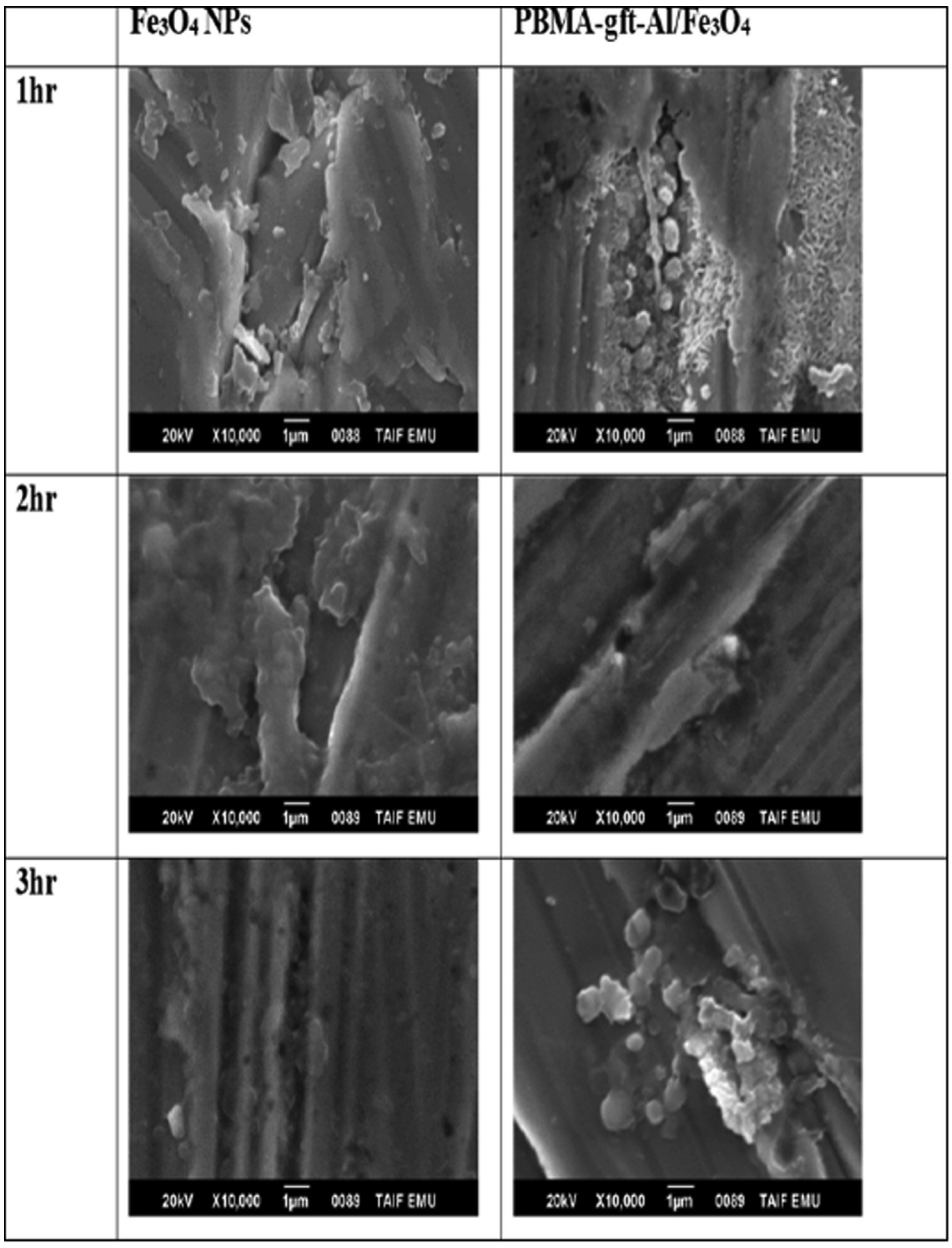

Fig. 11 SEM micrographs of a carbon steel surface after coating by Fe_3O_4 NPs and PBMA-gft-Al/Fe_3O_4 at different time.

the same as the effect of temperature due to the stability of the crystalline stage of the nanoparticles. The PBMA-gft-Alg/Fe_3O_4 2θ Peak values observed at 17° due to the presence of amorphous PBMA. The results indicate that PBMA-gft-Alg/Fe_3O_4 successfully synthesized as indicated in Fig. 14 (Bashtani et al., 2018).

3.3.7.5. The potentiodynamic polarization curves. Fig. 15 illustrated pre and post coating at (150 °C and 1hr, 2 hrs., 3 hrs.) with the nanocomposite and nanoparticles at zero time, acid molarity of 0.5. Table 3 showed the values of E_{corr}, i_{corr}, cathodic and anodic Tafel calculated from the curves. The curves representing that coated surfaces shift to lower current densities with greater negative potential values. The nanoparticles curve produced a lower effect compared to other coatings. Table 3 indicated the measured corrosion parameters curves. The data showed that the corrosion potentials and current densities inversely proportional. Also, the cathodic Tafel and polarization decreased after coating. This due to the polarization concentration reduction that reduced the metals dissolution and the electron production necessary to reduce cathodic reaction. This situation causes a buildup of O_2 at the cathode leading to polarization concentration. Fig. 15b and Table 3, illustrated that the nanoparticles coating slope at (150 °C, and 2hrs.) is higher that related to highest polarization and corrosion resistance. Fig. 15d and Table 3, indicated the coating cycle slope obtained using PBMA-gft-Alg/Fe_3O_4 at temperature of 150 °C, and 2 hrs. is greater due to the greatest polarization and corrosion resistance (Ibrahim & Bakdash, 2014).

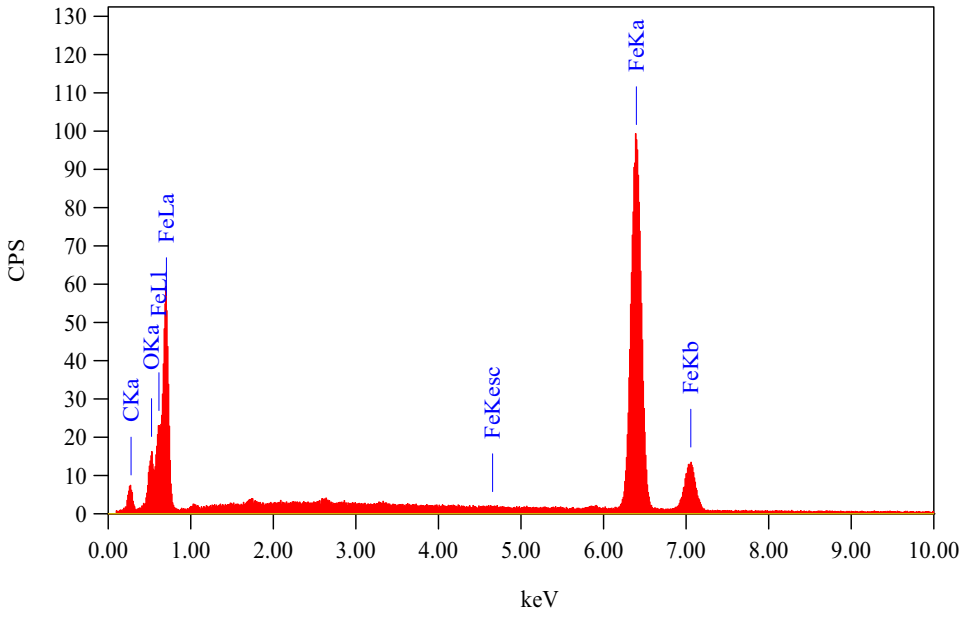

(a) Fe_3O_4 NPs at 1hr.

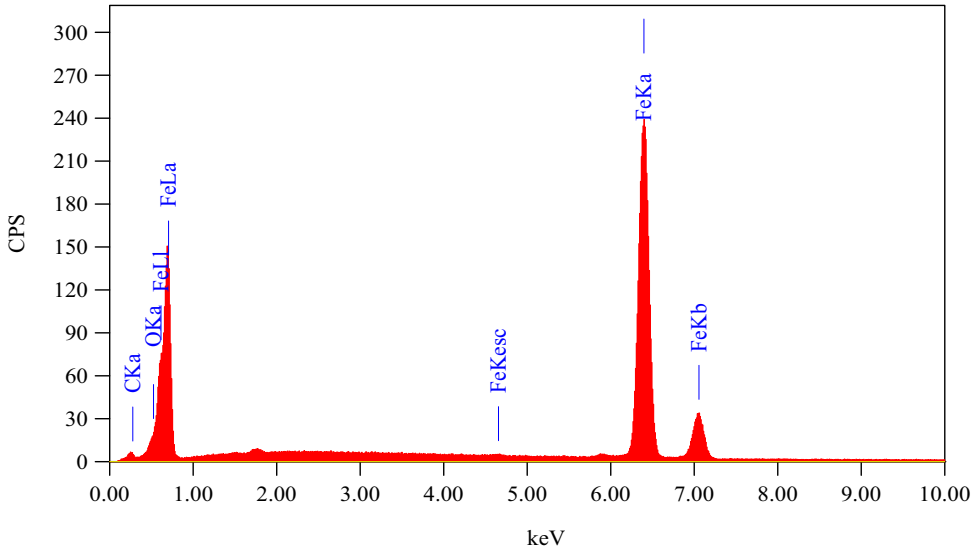

(b) PBMA-gft-Al/Fe_3O_4 at 1hr.

Fig. 12 EDS spectra related to surface of carbon steel after coating by Fe3O4 NPs PBMA-gft-Al/Fe3O4 nanocomposite at different time.

3.4. Examination using formation water/dyes

Fig. 16 and Table 4 showed that the surfaces coated with PBMA-gft-Alg/Fe_3O_4 in the formation water has lower current densities with more negative potential values. The PBMA-gft-Alg/Fe_3O_4 coated surfaces with MG and MB has lower current densities with more positive potential values.

Fig. 16b and Table 4 indicated that the PBMA-gft-Alg/Fe_3O_4 immersed in formation water at (150 °C, 2 hrs.) immersed in formation water slope is less than carbon steel coating cycle by PBMA-gft-Alg/Fe_3O_4 $_{at}$ (150 °C, 2 hrs.) in HCl, due to the greatest polarization and corrosion resistance. The PBMA-gft-Alg/Fe_3O_4 (150 °C, 2 hrs) slope of the coating in the PBMA-gft-Alg/Fe_3O_4 immersed in MG/MB at (150 °C,

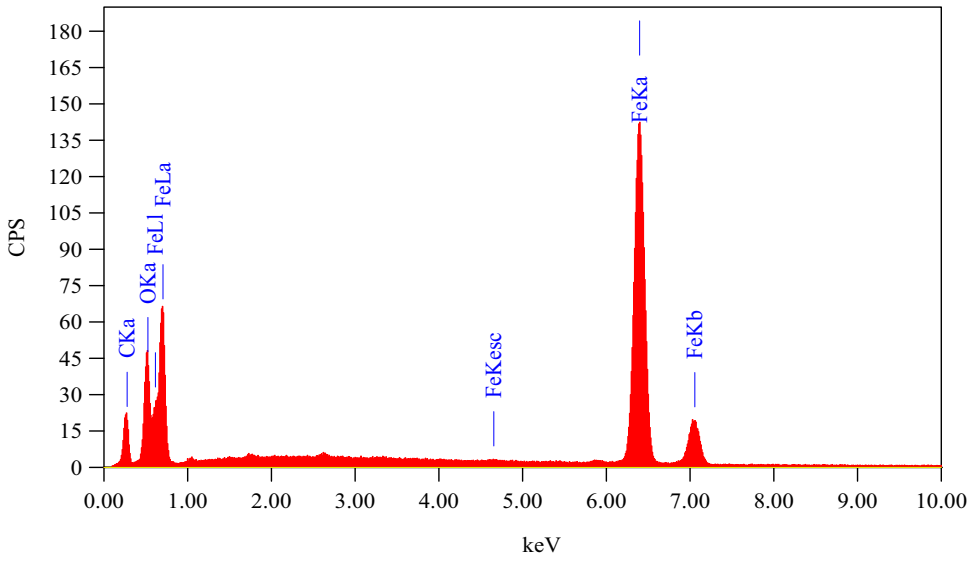

(c) Fe $_3O_4$ NPs at 2hrs.

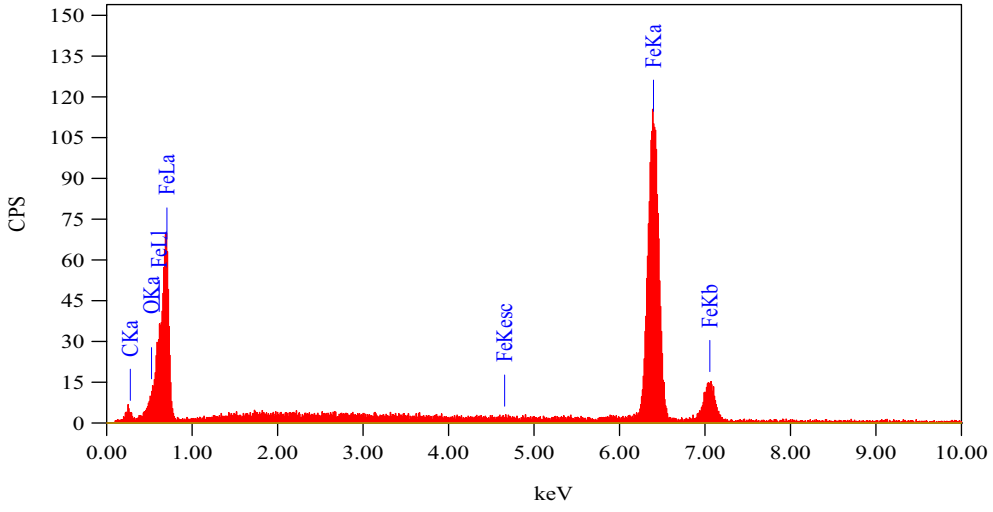

(d) PBMA-gft-Al/Fe_3O_4 at 2hrs.

Fig. 12 (*continued*)

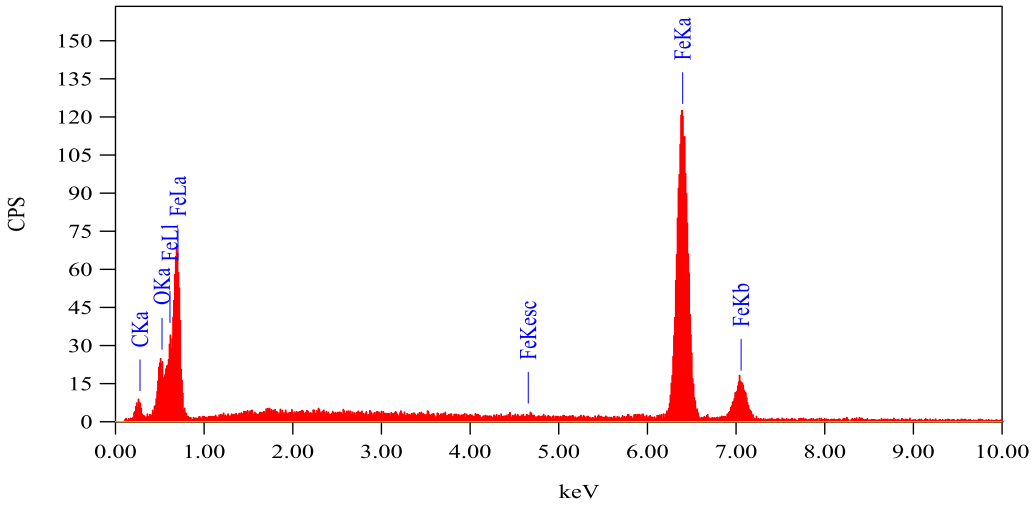

(e) Fe_3O_4 NPs at 2hrs.

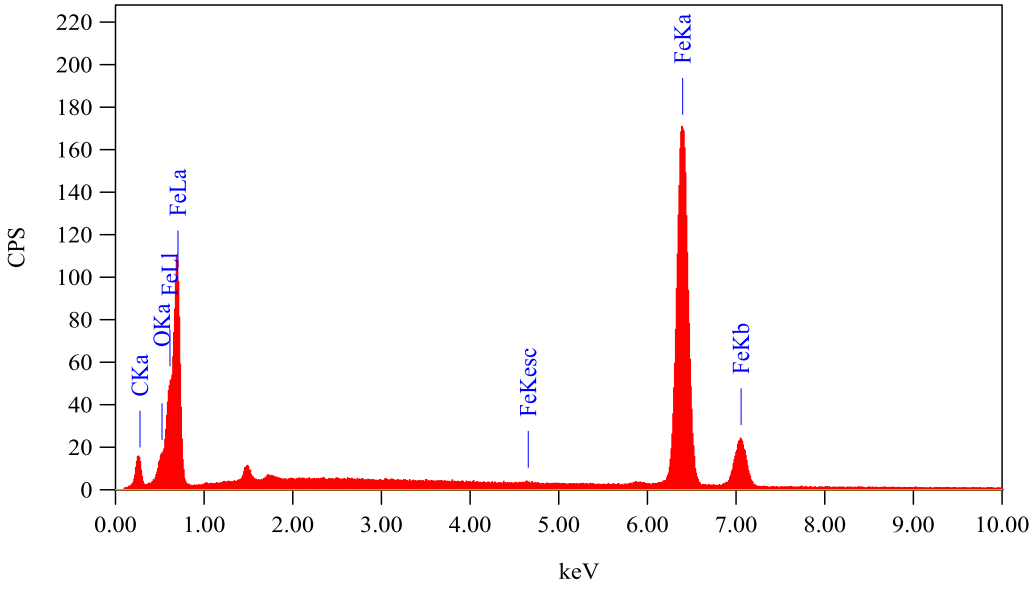

(f) PBMA-gft-Al/Fe_3O_4 at 2hrs.

Fig. 12 (*continued*)

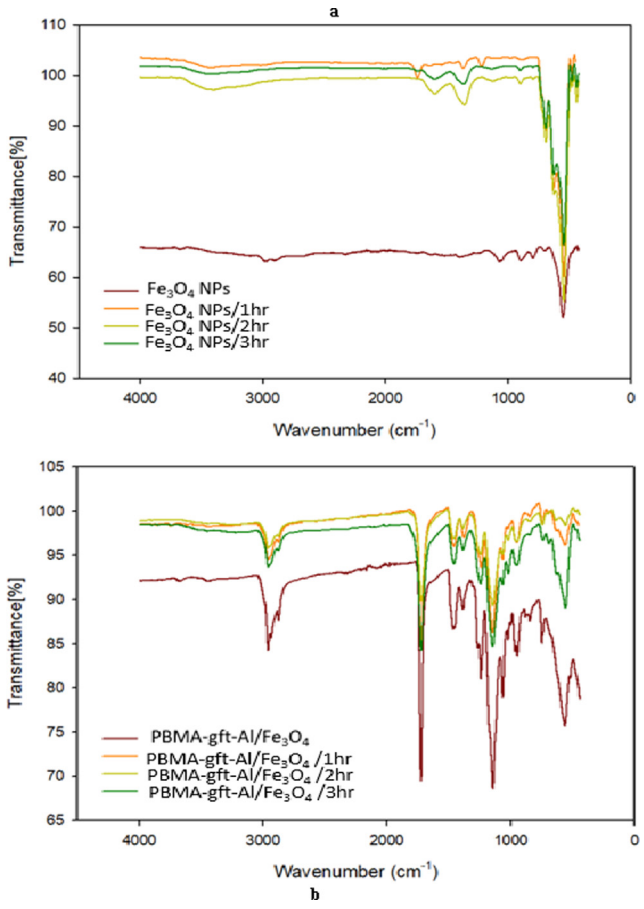

Fig. 13 FT-IR of Fe_3O_4 NPs and PBMA-gft-Al/Fe_3O_4 at different time hot-dib coating.

2 hrs.) is less than that of PBMA-gft-Alg/Fe_3O_4 immersed in the 0.5 M HCl at (150 °C, 2 hrs.) due to the greatest polarization/corrosion resistances.

4. Conclusions

1. Corrosion rate largely depended on the hydrochloric acid concentration and temperature.
2. Corrosion rate directly proportional to acid concentration and temperature.
3. Coating carbon steel by the HCl reduced corrosion.
4. PBMA-gft-Alg/Fe_3O_4 have superior coating quality compared to Fe_3O_4 NPs, and MG/MB respectively.
5. Electrochemical studies showed that both PBMA-gft-Alg/Fe_3O_4 and Fe_3O_4 NPs have good inhibiting properties for steel corrosion.
6. PBMA-gft-Alg/Fe_3O_4 is more effective in coating compared to the Fe_3O_4 NPs.
7. PBMA-gft-Alg/Fe_3O_4 have 99.9% corrosion resistance within the formation water corrosive medium.
8. PBMA-gft-Alg/Fe_3O_4 have 99.9% corrosion resistance within the MG and MB corrosive medium.

5. Data availability

The data used in this paper are available upon reasonable request from the corresponding author.

6. Additional points

No animals/humans were used for studies that are the basis of this research.

Declaration of Competing Interest

The authors declare that they have no known competing financial interests or personal relationships that could have appeared to influence the work reported in this paper.

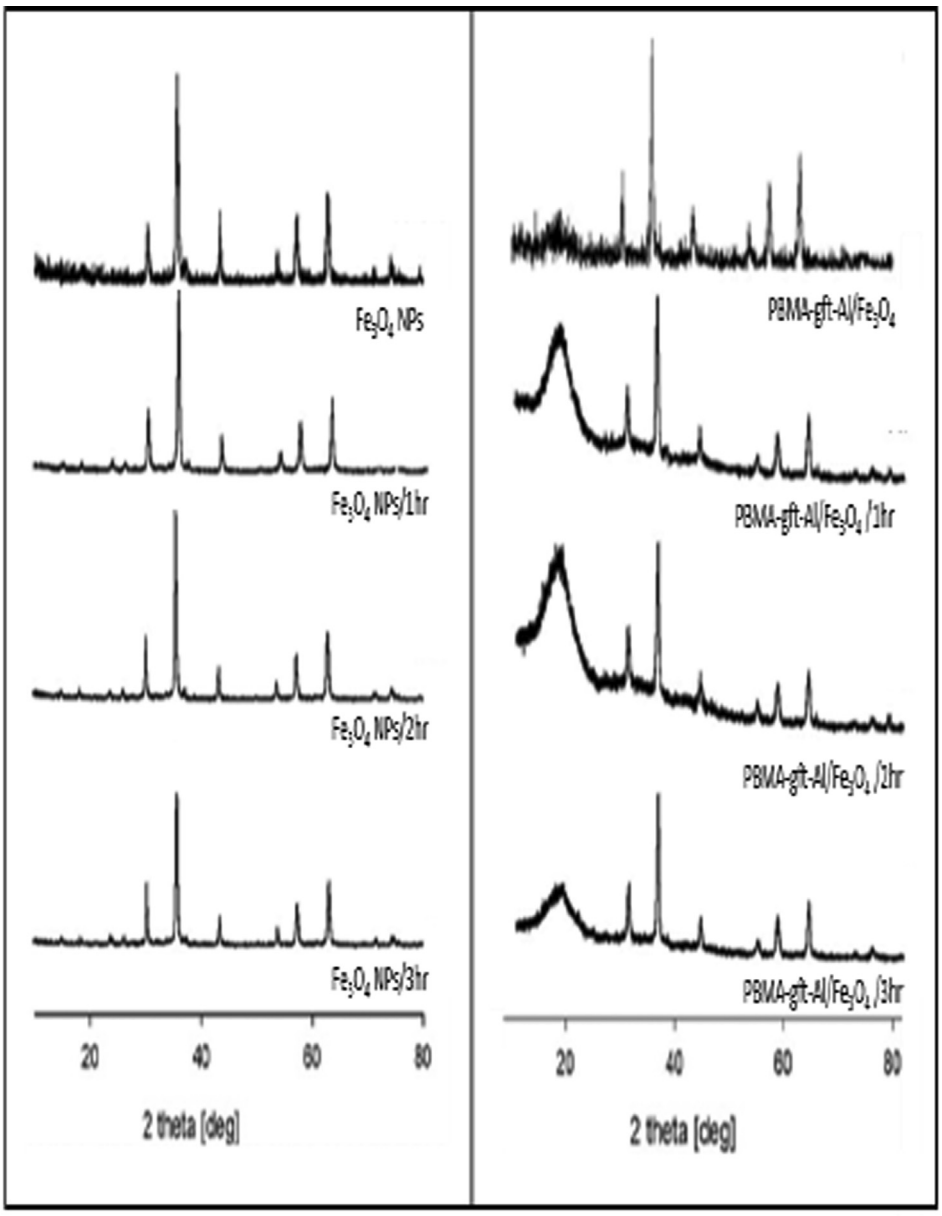

Fig. 14 X-ray diffraction patterns of Fe_3O_4 NPs and PBMA-gft-Alg/Fe_3O_4 at different time hot-dib coating.

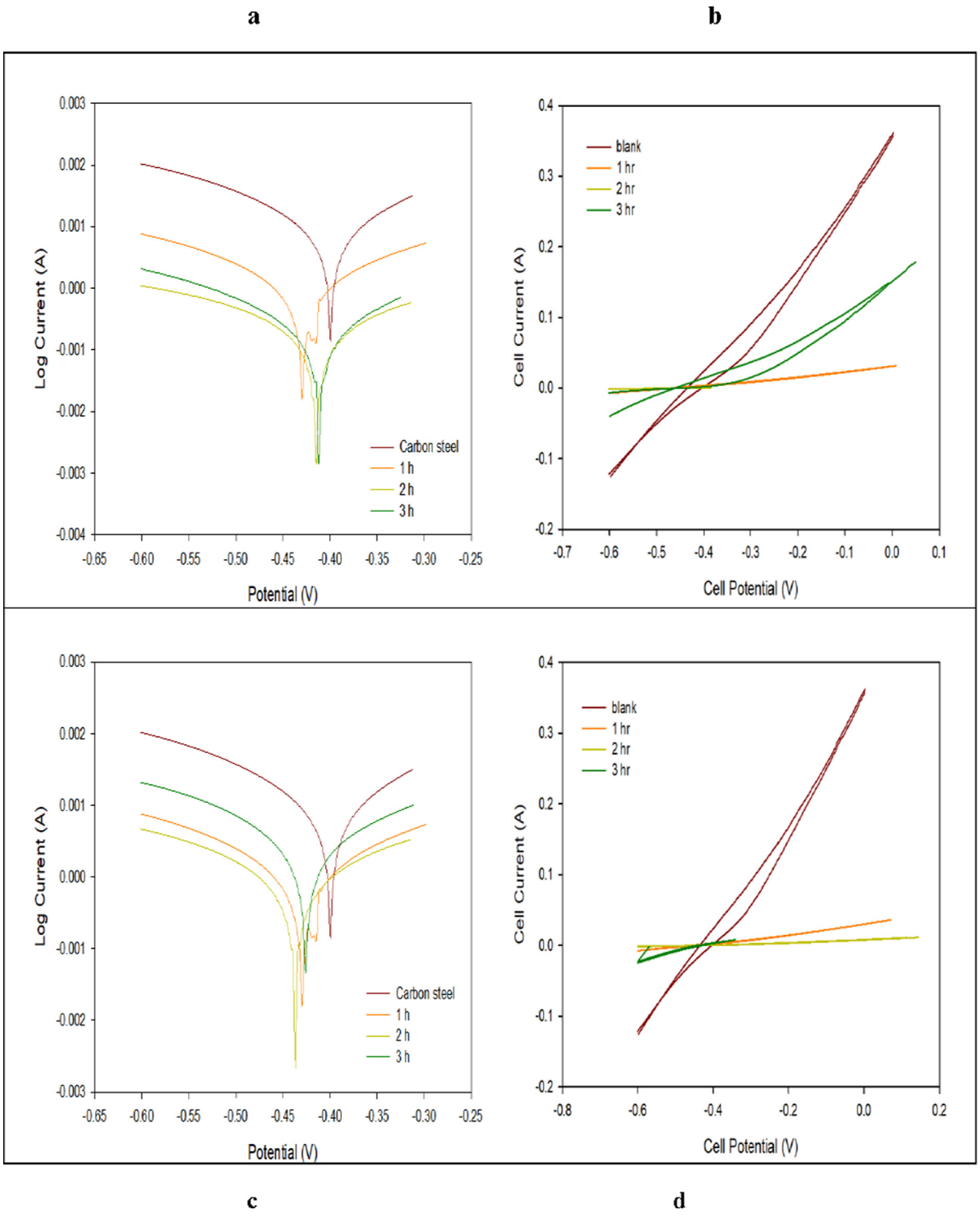

Fig. 15 Polarization curves and CV voltammograms of a carbon steel electrode in the absence and presence of coating by Fe_3O_4 NPs (above) and PBMA-gft-Alg/Fe_3O_4 (bottom) at different time at high corrosive condition.

Table 3 Potentiodynamic polarization parameters for corrosion carbon steel electrode in the absence and presence of coating by Fe_3O_4 NPs and PBMA-gft-Alg/Fe_3O_4 at different time at high corrosive condition.

		E_{corr} (V)	i_{corr} (A/cm^2)	PE%	Slope (A/V)	E_H (V)	E_P (V)
Carbon steel		−0.398	0.014.40	–	0.787	−0.670	−0.250
Carbon steel coating by Fe_3O_4 NPs at	1 hr	−0.454	0.001905	86.7%	0.062	0.030	−0.300
	2 hr	−0.411	0.000205	98.5%	0.006	0.001	−0.415
	3 hr	−0.408	0.000316	97.8%	0.289	0.014	−0.450
Carbon steel coating by PBMA-gft-Alg/Fe_3O_4 at	1 hr	−0.418	0.001230	91.0%	0.058	0.020	−0.020
	2 hr	−0.436	0.000197	98.6%	0.017	0.001	−0.198
	3 hr	−0.409	0.001849	97.9%	0.122	0.008	−0.493

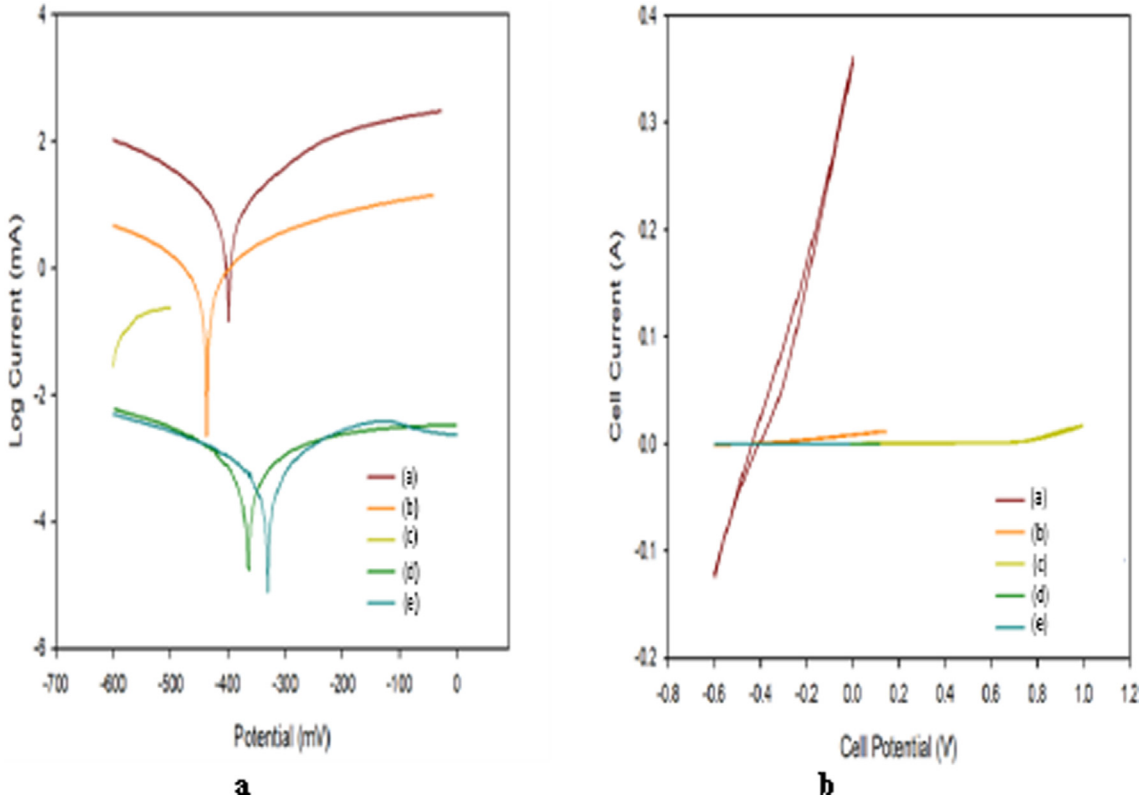

Fig. 16 Polarization curves and CV voltammograms of a carbon steel electrode (a) coating by PBMA-gft-Alg/Fe_3O_4 in HCl (b), coating by PBMA-gft-Alg/Fe_3O_4 in Formation water (c), coating by PBMA-gft-Alg/Fe_3O_4 in malachite green (d), coating by PBMA-gft-Alg/Fe_3O_4 in methylene blue (e).

Table 4 Potentiodynamic polarization parameters for corrosion of CARBON STEEL electrode immersed in a (0.5 M HCl) in the absence coating, and presence of coating PBMA-gft-Alg/Fe_3O_4 in (HCl, Formation water, MG, MB).

	E_{corr} (V)	i_{corr} (A)	IE%	Slope (A/V)	E_H (v)	E_P (v)
Blank	−0.398	0.014.4	–	0.787	−0.670	−0.250
In HCl	−0.436	0.000197	98.6%	0.017	0.001	−0.198
Formation water	−0.556	0.000114	99.2%	0.005	1.000	0.583
MG	−0.346	6.285×10^{-8}	99.8%	1×10^{-06}	0.116	−0.133
MB	−0.340	5.874×10^{-8}	99.9%	1×10^{-05}	−0.012	0.018

Acknowledgments

The author acknowledges the support of Taif University Researchers Supporting Project number TURSP-2020/136, Taif University, Taif, Saudi Arabia.

References

Ahmaeed, W.N., Abd, A.N., Khadom, A.A., 2019. Corrosion inhibition effect of sodium iodide for mild steel in 1 m hydrochloric acid: gravimetrical and electrochemical studies. International Journal of Corrosion and Scale Prevention 4, 1097–1111.

Alam, A., Zhang, Y., Kuan, H.-C., Lee, S.-H., Ma, J., 2018. Polymer composite hydrogels containing carbon nanomaterials—Morphology and mechanical and functional performance. Prog. Polym. Sci. 77, 1–18.

Alzahrani, E., Abo-Dief, H.M., Algethami, F., 2020. Poly (butyl methacrylate)-grafted alginate/Fe3O4 nanocomposite: Synthesis and its application for removal of dyes. J. Chin. Chem. Soc.

Aslam, J., Aslam, R., Alrefaee, S., 2020. Gravimetric, electrochemical, and morphological studies of an isoxazole derivative as corrosion inhibitor for mild steel in 1M HCl. *Arabian Journal* **of Chemistry** 13 (11), 7744–7758.

Bashtani, E., Amiri, A., Baghayeri, M., 2018. A nanocomposite consisting of poly (methyl methacrylate), graphene oxide and Fe 3 O 4 nanoparticles as a sorbent for magnetic solid-phase extraction of aromatic amines. Microchim. Acta 185 (1), 14.

Bertolini, L., Elsener, B., Pedeferri, P., & Polder, R. (2004). Corrosion of Steel in Concrete–Prevention, Diagnosis and Repair. Wieley–VCH. In: Weinheim.

Bordbar, A., Rastegari, A., Amiri, R., Ranjbakhsh, E., Abbasi, M., Khosropour, A., 2014. 2014. Characterization of modified magnetite nanoparticles for albumin immobilization, Biotechnology research international.

Cui, X., Zhu, G., Pan, Y., Shao, Q., Dong, M., Zhang, Y., Guo, Z., 2018. Polydimethylsiloxane-titania nanocomposite coating: fabrication and corrosion resistance. Polymer 138, 203–210.

Deyab, M., 2015. Effect of carbon nano-tubes on the corrosion resistance of alkyd coating immersed in sodium chloride solution. Prog. Org. Coat. 85, 146–150.

Dwivedi, D., Lepková, K., Becker, T., 2017. Carbon steel corrosion: a review of key surface properties and characterization methods. RSC Adv. 7 (8), 4580–4610.

Elmorsi, M., Hassanein, A., 1999. Corrosion inhibition of copper by heterocyclic compounds. Corros. Sci. 41 (12), 2337–2352.

Ershad-Langroudi, A., Abdollahi, H., Rahimi, A., 2017. Mechanical properties of sol–gel prepared nanocomposite coatings in the presence of titania and alumina-derived nanoparticles. Plast., Rubber Compos. 46 (1), 25–34.

Fawzy, A., Zaafarany, I., Ali, H., Abdallah, M., 2018. New synthesized amino acids-based surfactants as efficient inhibitors for corrosion of mild Steel in hydrochloric acid medium: kinetics and thermodynamic approach. Int. J. Electrochem. Sci 13 (5), 4575–4600.

Gray, J., Luan, B., 2002. Protective coatings on magnesium and its alloys—a critical review. J. Alloy. Compd. 336 (1–2), 88–113.

Guan, L.-Z., Zhao, L., Wan, Y.-J., Tang, L.-C., 2018. Three-dimensional graphene-based polymer nanocomposites: preparation, properties and applications. Nanoscale 10 (31), 14788–14811.

Haque, J., Srivastava, V., Verma, C., Lgaz, Z., Salghi, R., Quraishi, M. N-Methyl-N,N,N-trioctylammonium chloride as a novel and green corrosion inhibitor for mild steel in an acid chloride medium: electrochemical, DFT and MD studies. New J. Chem., 41, 13647-13662

Harb, S.V., Trentin, A., de Souza, T.A.C., Magnani, M., Pulcinelli, S. H., Santilli, C.V., Hammer, P., 2020. Effective corrosion protection by eco-friendly self-healing PMMA-cerium oxide coatings. Chem. Eng. J. 383, 123219.

Horwood, E. Corrosion in sea water systems. In.

Hussein-Al-Ali, S. H., El Zowalaty, M. E., Kura, A. U., Geilich, B., Fakurazi, S., Webster, T. J., & Hussein, M. Z. (2014). Antimicrobial and controlled release studies of a novel nystatin conjugated iron oxide nanocomposite. BioMed research international, 2014.

Hu, K., Zhuang, J., Ding, J., Ma, Z., Wang, F., Zeng, X. Influence of biomacromolecule DNA corrosion inhibitor on carbon steel. Corrosion Science, 125, 68-76.

Ibrahim, M., Bakdash, R., 2014. Zinc coatings of high hardness on steel by electrodeposition from glutamate complex baths. Transactions of the IMF 92 (4), 218–226.

Jagtap, S.B., Patil, V.D., Suresh, K., Ram, F., Mohan, M.S., Rajput, S.S., Shanmuganathan, K., 2018. Functionalized carbon nanotube reinforced polymer nanocomposite microcapsules with enhanced stiffness. Colloids Surf., A 550, 82–89.

Joshi, M., Adak, B., Butola, B., 2018. Polyurethane nanocomposite based gas barrier films, membranes and coatings: A review on synthesis, characterization and potential applications. Prog. Mater Sci. 97, 230–282.

Keera, S., Deyab, M., 2005. Effect of some organic surfactants on the electrochemical behaviour of carbon steel in formation water. Colloids Surf., A 266 (1–3), 129–140.

Ledwig, P., Dubiel, B., 2017. Microstructure and corrosion resistance of composite nc-TiO2/Ni coating on 316L steel. Arch. Metall. Mater.

Lin, J., Dahan, I., 2015. Nanostructured chromium coatings with enhanced mechanical properties and corrosion resistance. Surf. Coat. Technol. 265, 154–159.

Mai, Y., Yu, Z., 2006. Polymer Nanocomposites. Yu.–Publishing Limited, Cambridge.

Mittal, A., Ahmad, R., Hasan, I., 2016. Poly (methyl methacrylate)-grafted alginate/Fe3O4 nanocomposite: synthesis and its application for the removal of heavy metal ions. Desalin. Water Treat. 57 (42), 19820–19833.

Mora, L.V., Naik, S., Paul, S., Dawson, R., Neville, A., Barker, R., 2017. Influence of silica nanoparticles on corrosion resistance of sol-gel based coatings on mild steel. Surf. Coat. Technol. 324, 368–375.

Morton, D., Madaleno, L., Chaloner-Gill, B., Quintero, M., Al-Borno, A., 2018. Volumetric superhydrophobic coatings for offshore corrosion protection. Paper presented at the NACE International Corrosion Conference Proceedings.

Nagiub, A., Mahross, M., Khalil, H., Mahran, B., Yehia, M., El-Sabbah, M., 2013. Azo dye compounds as corrosion inhibitors for dissolution of mild steel in hydrochloric acid solution. Portugaliae Electrochimica Acta 31 (2), 119–139.

Nguyen-Tri, P., Nguyen, T. A., Carriere, P., & Ngo Xuan, C. (2018). Nanocomposite coatings: preparation, characterization, properties, and applications. International Journal of Corrosion, 2018.

Oguzie, E., Okolue, B., Ogukwe, C., Unaegbu, C., 2006. Corrosion inhibition and adsorption behaviour of bismark brown dye on aluminium in sodium hydroxide solution. Mater. Lett. 60 (28), 3376–3378.

Osarolube, E., Owate, I., Oforka, N., 2008. Corrosion behaviour of mild and high carbon steels in various acidic media. Scientific Research and Essay 3 (6), 224–228.

Peng, B., Tang, J., Luo, J., Wang, P., Ding, B., Tam, K.C., 2018. Applications of nanotechnology in oil and gas industry: Progress and perspective. The Canadian journal of chemical engineering 96 (1), 91–100.

Qu, X., Alvarez, P.J., Li, Q., 2013. Applications of nanotechnology in water and wastewater treatment. Water Res. 47 (12), 3931–3946.

Radhamani, A., Lau, H.C., Ramakrishna, S., 2020. Nanocomposite coatings on steel for enhancing the corrosion resistance: A review. J. Compos. Mater. 54 (5), 681–701.

Ramezanzadeh, B., Niroumandrad, S., Ahmadi, A., Mahdavian, M., Moghadam, M.M., 2016. Enhancement of barrier and corrosion protection performance of an epoxy coating through wet transfer of amino functionalized graphene oxide. Corros. Sci. 103, 283–304.

Sanchez, C., Belleville, P., Popall, M., Nicole, L., 2011. Applications of advanced hybrid organic–inorganic nanomaterials: from laboratory to market. Chem. Soc. Rev. 40 (2), 696–753.

Sneha, M., Sundaram, N.M., 2015. Preparation and characterization of an iron oxide-hydroxyapatite nanocomposite for potential bone cancer therapy. Int. J. Nanomed. 10 (Suppl 1), 99.

Srivastava, V., Haque, J., Verma, C., Singh, P., Lgaz, H., Salghi, R., Quraishi, M., 2017. Amino acid based imidazolium zwitterions as novel and green corrosion inhibitors for mild steel: Experimental, DFT and MD studies. J. Mol. Liq. 244, 340–352.

Tang, J., Shao, Y., Zhang, T., Meng, G., Wang, F., 2011. Corrosion behaviour of carbon steel in different concentrations of HCl solutions containing H2S at 90 C. Corros. Sci. 53 (5), 1715–1723.

Waldron, R., 1955. Infrared spectra of ferrites. *Physical review* 99 (6), 1727.

Wang, J., Zhang, T., Zhang, X., Asif, M., Jiang, L., Dong, S., Liu, H., 2020. Inhibition effects of benzalkonium chloride on Chlorella vulgaris induced corrosion of carbon steel. J. Mater. Sci. Technol. 43, 14–20.

Xiang, T., Han, Y., Guo, Z., Wang, R., Zheng, S., Li, S., Dai, X., 2018. Fabrication of inherent anticorrosion superhydrophobic surfaces on metals. ACS Sustainable Chem. Eng. 6 (4), 5598–5606.

Yao, B., Ni, C., Xiong, C., Zhu, C., Huang, B., 2010. Hydrophobic modification of sodium alginate and its application in drug controlled release. Bioprocess Biosyst. Eng. 33 (4), 457–463.

Ye, Y., Chen, H., Zou, Y., Zhao, H., 2021. Study on self-healing and corrosion resistance behaviors of functionalized carbon dot-intercalated graphene-based waterborne epoxy coating. J. Mater. Sci. Technol. 67, 226–236.

Ye, Y., Yang, D., Chen, H., Guo, S., Wang, L., 2020. A high-efficiency corrosion inhibitor of N-doped citric acid-based carbon dots for mild steel in hydrochloric acid environment. J. Hazard. Mater. 381, 121019.

Yusoff, M.H., Azmi, M.N., Hussin, M.H., Osman, H., Raja, P.B., Rahim, A.A., Awang, K., 2020. An Electrochemical Evaluation of Synthesized Coumarin-Azo Dyes as Potential Corrosion Inhibitors for Mild Steel in 1 M HCl Medium. Int. J. Electrochem. Sci 15, 11742–11756.

Zhang, D., Wang, L., Qian, H., Li, X., 2016. Superhydrophobic surfaces for corrosion protection: a review of recent progresses and future directions. J. Coat. Technol. Res. 13 (1), 11–29.